Measurement of the Branching Ratio, Lepton Angular Distribution and Determination of CKM Matrix element $|V_{cb}|$ in Inclusive $B \to X_c \ell \nu$ Semileptonic Decays at Belle II

Rajeshwari Roy

Masterarbeit in Physik
angefertigt im Physikalischen Institut

vorgelegt der
Mathematisch-Naturwissenschaftlichen Fakultät
der
Rheinischen Friedrich-Wilhelms-Universität
Bonn

March 2026

I hereby declare that this thesis was formulated by myself and that no sources or tools other than those cited were used.

Bonn, 16.03.2026 .... Rajeshwari Roy

Date — Signature

1. Gutachter: Prof. Dr. Florian U. Bernlochner
2. Gutachter: Dr. Markus T. Prim

Acknowledgements

I would like to sincerely thank my supervisors, **Prof. Dr. Florian Bernlochner** and **Dr. Markus Prim** for giving me an opportunity to be a part of this analysis and for their continuous guidance, insightful discussions, and unwavering support throughout this project. Their clarity in both theoretical and experimental aspects of flavor physics greatly shaped this work and deepened my understanding of the subject.

I am especially grateful to **Munira Khan** for her invaluable day-to-day guidance, patience, and constant encouragement. Her support in navigating the analysis framework was essential to the successful completion of this thesis. The many detailed discussions and her readiness to help at every stage made a tremendous difference. I am thankful to **Ilias Tsaklidis** and **Agrim Aggarwal** for their help in setting up and in understanding the `SysVar` framework. Their support in implementing and validating the systematic uncertainty treatment was greatly appreciated. I would also like to thank all members of the working group in Bonn for their helpful discussions and for the consistent and constructive feedback during our weekly meetings. The collaborative environment and open exchange of ideas significantly improved the quality of this work.

Finally, I would like to express my deepest gratitude to my parents for giving me the opportunity and support to pursue my Master's degree at the University of Bonn. Their encouragement, sacrifices, and constant belief in me made this journey possible. I am also thankful to my friends for their support and motivation throughout this time.

I truly appreciate the time, mentorship, and encouragement that all of you have invested in me throughout this project.

Contents

CHAPTER 1

Introduction

The study of semileptonic decays of heavy mesons plays a central role in testing the Standard Model (SM) of particle physics and in determining its fundamental parameters. In particular, decays of the B meson provide a unique laboratory for probing the dynamics of the weak interactions and the structure of the Cabibbo–Kobayashi–Maskawa (CKM) quark-mixing matrix, which encodes the strengths of flavor-changing weak transitions among quarks. Precise measurements of B meson decay properties are therefore essential for validating the internal consistency of the SM and for searching for possible signatures of physics beyond it.

Among B meson decay modes, inclusive semileptonic decays of the form

$$B \to X_c \ell \nu \tag{1.1}$$

where X_c denotes any charmed hadronic final state, ℓ a charged lepton, and ν, the corresponding neutrino and are of particular theoretical and experimental importance. These decays are experimentally clean due to the presence of a high-momentum charged lepton and are theoretically well described using the framework of Heavy Quark Expansion (HQE), which introduces non-perturbative corrections from $\mathcal{O}(1/m_b^2)$. As a result, inclusive semileptonic decays allow for a relatively model-independent determination of the CKM matrix element $|V_{cb}|$, that governs transitions between bottom and charm quarks. Since there is no dependence on the exclusive hadronic form factors in inclusive decays, the measurement of $|V_{cb}|$ is clean. The study of the "moments" including the invariant mass M_X, square of the momentum transfer q^2 and the lepton energy (momentum) E_ℓ (p_ℓ) gives us knowledge about the non-perturbative HQE dynamics.

The measurement of the differential and absolute branching ratios of $B \to X_c \ell \nu$ decays provides important input for the determination of the CKM matrix element $|V_{cb}|$. Inclusive determinations of $|V_{cb}|$ relying on the HQE and exclusive determinations that are based on specific hadronic form factors, currently exhibit a persistent tension. By measuring the partial branching fractions and kinematic distributions with improved precision, this analysis provides additional constraints on the modeling of semileptonic B decays and on the parameters entering the HQE fits. These improved experimental inputs help refine the inclusive determination of $|V_{cb}|$ and contribute to clarifying the origin of the inclusive-exclusive tension.

In addition to the total decay rate, the angular distribution of the emitted charged lepton offers deeper insight into the underlying weak interaction structure. The lepton angular distribution is sensitive to the helicity structure of the weak current and provides an important test of the V–A nature of the charged current interaction predicted by the SM.

The first part of this thesis deals with the reconstruction of the inclusive $B \to X_c \ell \nu$ decays using hadronic tagging. After having separated the signal and background events, resolution studies are performed as explained in Sec. 5. The effect of the final-state radiation photons on the kinematic variables for electrons and muons is investigated. Further, studying the B_{tag} momentum is essential as it enables full event reconstruction of the signal-side B meson, suppresses backgrounds, validates detector modeling, and directly controls the $|V_{cb}|$ precision measurements. Further, the production of migration matrices of the kinematic variables quantifies how true/generated Monte Carlo (MC) quantities migrate into reconstructed (detector-level) MC quantities because of detector effects. This is then used in the process of unfolding, where the measured kinematic variable is corrected back to its truth level. In the further chapters, we investigate the acceptance efficiencies of the detector, which is incorporated in the unfolding procedure. For the process of unfolding, the lepton momentum p_ℓ, momentum transfer squared q^2 and the helicity angle $\cos\,\theta_\ell$ is modeled into a 3-bin fit of the invariant mass of the charm hadronic system M_X. A binned maximum likelihood fit is carried out using a `pyhf` statistical model. This model incorporates separate templates for the signal ($B \to X_c \ell \nu$), background, and continuum background components, each described in Sec. 4.2.1, Sec. 4.2.2 and Sec. 4.2.3 respectively. The signal yields thus obtained from the template fitting model along with the migration matrices and the efficiency corrections help construct the exact unfolded distribution of the kinematic variables taken into consideration and is eventually used in the differential and absolute branching ratio calculations. The `cabinetry` framework is utilized to manage the model construction, parameterization of statistical and systematic uncertainties, and fitting workflow.

The second part of this analysis consists of the measurement of the differential and the absolute B meson branching ratio for the $B \to X_c \ell \nu$ semileptonic decay taking the statistical and the systematic uncertainties into account. The statistical uncertainties are obtained from the signal fitting template. In order to calculate the contribution of each systematic uncertainty (branching fractions, tracking, FEI tag-side efficiency, lepton identification corrections, form factors), the `SysVar` framework is used. The brief working and overview of `Sysvar` can be found in Sec. 2.2.6. The variations for each of the systematics are incorporated as nuisance parameters in the overall fitting model.

In the last chapter, we employ the `Kolya` package [1] to fit the experimental moments in order to extract the CKM matrix element $|V_{cb}|$ together with the HQE parameters. The framework computes theoretical predictions for the moments and for the inclusive semileptonic B-meson decay rate within the kinematic scheme. The fit includes non-perturbative corrections up to $\mathcal{O}(1/m_b^3)$ and accounts for perturbative QCD corrections. A χ^2 minimization is performed in order to determine the values that best reproduce the measured moments, while consistently accounting for experimental uncertainties and their correlations.

Therefore, the results presented in this analysis help strengthen the experimental foundations of the SM and support ongoing efforts to uncover potential physics beyond it.

CHAPTER 2

Theory

This chapter presents the theoretical framework for the study of inclusive $B \to X_c \ell \nu$ decays, together with the statistical methodology employed in this thesis. It introduces the relevant decays and kinematic observables, outlining the statistical techniques used to extract the physical parameters of interest.

2.1 Physics Foundation

The physics foundations underlying this thesis are based on the principles of particle and nuclear physics as presented in [2]. The introduction to the theoretical structure of the SM, with particular emphasis on weak interactions, quark flavor physics, and the role of the CKM matrix in describing quark mixing and semileptonic decays form the basic building blocks. The essential treatment of hadronic structure, heavy-quark dynamics, and decay kinematics helps in the analysis of B-meson processes [3]. Together Ref. [2, 4, 5] form a coherent theoretical and statistical basis for understanding inclusive $B \to X_c \ell \nu$ decays and for interpreting the results of the analysis within the broader framework of contemporary particle physics.

2.2 Statistical Tools

This section compiles an overview of the statistical methods and techniques taken that were used in this thesis.

2.2.1 Maximum Likelihood

The method of maximum likelihood (ML) is a widely used technique for parameter estimation in statistical data analysis. Given a set of independent observations $\mathbf{x} = (x_1, \ldots, x_n)$ described by a probability density function $f(x \mid \theta)$, the likelihood function is defined as

$$\mathscr{L}(\theta) = \prod_{i=1}^{n} f(x_i \mid \theta), \tag{2.1}$$

or, equivalently, in terms of the log-likelihood,

$$\ln \mathscr{L}(\theta) = \sum_{i=1}^{n} \ln f(x_i \mid \theta). \tag{2.2}$$

The ML estimator $\hat{\theta}$ is obtained by maximizing $\mathscr{L}$ (or $\ln \mathscr{L}$) with respect to the model parameters. Under general regularity conditions and for sufficiently large data samples, ML estimators are consistent, asymptotically unbiased, and efficient, with variances approaching the Cramér–Rao–Fréchet lower bound,

$$\mathrm{Var}(\hat{\theta}) \geq \frac{1}{I(\theta)}, \qquad I(\theta) = -\mathbb{E}\left[\frac{\partial^2 \ln \mathscr{L}}{\partial \theta^2}\right], \tag{2.3}$$

where $I(\theta)$ denotes the Fisher information.

The statistical uncertainty on an ML estimator can be approximated from the curvature of the log-likelihood at its maximum,

$$\sigma_{\hat{\theta}}^2 \approx \left(-\frac{\partial^2 \ln \mathscr{L}}{\partial \theta^2}\right)^{-1}_{\theta=\hat{\theta}}, \tag{2.4}$$

and extended to multi-parameter cases using the inverse Fisher information matrix. The ML framework naturally generalizes to extended likelihoods, which include the total number of observed events, and to binned data using Poisson statistics [5].

2.2.2 `pyhf`

The statistical analysis in this work is performed using `pyhf` [6], a Python-based framework for likelihood-based inference widely adopted in high-energy physics. The `pyhf` library provides a pure-Python implementation of the HistFactory[7] statistical model, enabling the construction of binned likelihood functions that combine signal and background expectations with systematic uncertainties encoded as nuisance parameters. In this framework, observed event counts in each bin are modeled using Poisson statistics, while systematic effects are incorporated through constraint terms. The analysis is carried out by profiling the likelihood with respect to nuisance parameters. `pyhf` facilitates reproducible and scalable statistical analyses consistent with the standard frequentist methodology.

2.2.3 `cabinetry`

The statistical analysis workflow is organized using `cabinetry` [8], a high-level Python framework built on top of `pyhf` to streamline the construction and execution of likelihood-based analyses in high-energy physics. `cabinetry` provides a configuration-driven approach, typically to define datasets, model components, and systematic uncertainties. It automates tasks such as template modeling, parameter fitting, hypothesis testing, and result visualization while internally relying on the `pyhf` statistical engine for likelihood evaluation and inference. `cabinetry` therefore separates complex analysis configurations from implementation details.

2.2.4 Monte-Carlo Simulations

MC simulations play a central role in High-Energy Physics (HEP) measurements. At Belle II, starting from the decay of the $\Upsilon(4S)$ meson, all subsequent physical interactions and decay chains up to the final detector response are modeled using stochastic event generation. Each simulated event is assigned randomly according to the experimentally established probability distributions. The event generation follows the fundamental principles of particle physics within the SM framework and incorporates a detailed description of the detector's characteristics. When a sufficiently large sample of events is produced, the simulation enables an in-depth investigation of complex physical phenomena. Owing to statistical principles, increasing the number of simulated events enhances the precision and reliability of the analysis. As a result, physical parameters and their associated uncertainties can be extracted and directly compared with experimental measurements, allowing potential deviations between MC simulations and real data.

Simulated samples are used to model signal and background processes, determine selection efficiencies, and construct the probability density functions employed in the fit.
In addition, MC samples are used to construct Asimov datasets and perform statistical tests, allowing validation of the fit strategy and determination of the expected sensitivity and uncertainties. Systematic uncertainties associated with modeling assumptions and limited MC statistics are evaluated by varying the relevant parameters within their uncertainties and propagating the effects to the final measurement.

2.2.5 Asimov Data

Asimov data refers to an idealized dataset constructed such that the observed event counts are equal to their expectation values under a given statistical model. Instead of being generated through random sampling, the Asimov dataset is defined deterministically by setting the observed data in each bin to the mean prediction of the model for a chosen set of parameter values, typically corresponding to the nominal or null hypothesis. As a result, statistical fluctuations are absent, and the ML estimator coincides exactly with the assumed parameter values. The use of Asimov datasets enables validation of the fit model, checking for intrinsic biases, and helps determine the expected sensitivity and uncertainty of measurements without taking statistical fluctuations into account [9].

2.2.6 `SysVar`

A way to incorporate and handle systematic uncertainties and their correlations is using the `SysVar` framework, a Python-based tool designed to ensure a consistent treatment of shape and normalization systematics in HEP analyses. `SysVar` operates at the level of event weights and templates, allowing Data/MC correction factors to be applied directly to dataframes and their corresponding systematic variations to be propagated to binned templates. To account for potentially complex and arbitrary correlations across bins, templates, and reconstruction channels, `SysVar` constructs a global covariance matrix with dimensions of the channels, templates and bins and performs an eigenvalue decomposition. The resulting eigenvariations define orthogonal nuisance parameters that encode fully correlated shape variations across all affected bins, enabling their consistent inclusion in simultaneous template fits. For a detailed description of the working and documentation of `SysVar`, the reader should refer to [10] (technical talk at the analysis tools meeting) and to the documentation in [11]. In this analysis, eigenvariations for every systematic uncertainty is generated using `SysVar` and then used in the `pyhf` model as nuisance parameters to generate the overall uncertainty contribution from a particular systematic.

CHAPTER 3

Experimental Setup

3.1 Belle II Detector

The Belle II detector is a general-purpose 4π detector designed for the B-factory experiment which utilizes high-precision measurements of B Meson decays to validate predictions of the SM and to explore possible indications of new physics through deviations from SM expectations. It is carried out at the SuperKEKB e^+e^- accelerator located at KEK, Japan.

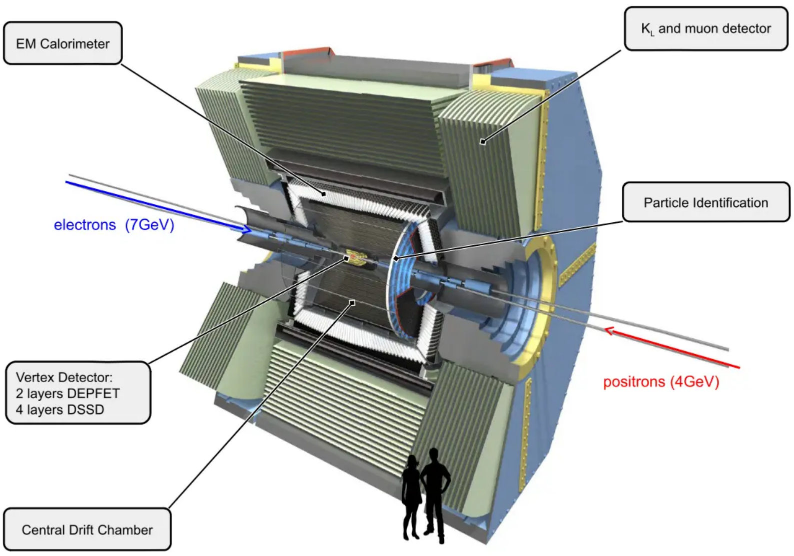

Figure 3.1: Overview of the Belle II detector.[12]

It is optimized for the precise reconstruction of particles produced in electron-positron collisions and consists of several sub-detector systems arranged in a cylindrical geometry around the interaction point. The innermost tracking system comprises of two layers of pixelated silicon detectors (PXD) followed by four layers of double-sided silicon strip detectors (SVD), providing excellent vertex resolution for the reconstruction of B mesons. Surrounding the vertex detector is a central drift chamber (CDC), which measures the trajectories, momenta, and specific ionization energy loss of charged particles. Particle identification is performed using a Time-Of-Propagation (TOP) counter in the barrel region and an aerogel ring-imaging Cherenkov detector (A-RICH) in the forward endcap. An electromagnetic calorimeter (ECL), composed of scintillating crystals is used to measure the energy deposition in the form of electromagnetic (EM) showers of electrons and photons. All sub-detectors are enclosed within a superconducting solenoid providing a uniform magnetic field of 1.5 T which causes the bending of the path of the charged particles as a result of the Lorentz force. The outside of the solenoid is instrumented with detectors for muon identification and K_L^0 meson detection (KLM), completing the full event reconstruction capabilities of the Belle II detector.

The electrons e^- and positrons e^+ are accelerated in opposite directions using energy beams E_{e^-}= 7 GeV and E_{e^+}= 4 GeV, which results in E_{CMS} = 10.58 GeV that is close to the mass of the $\Upsilon(4S)$ resonance. The asymmetry in the beams results in a boost of the $\Upsilon(4S)$ along the beam axis, which then dominantly decays into B meson pairs. The B mesons then follow several decay chains, producing various final-state particle systems.

3.2 Data Samples and MC Modelling

This analysis is performed on the Long Shutdown 1 (LS1) data sample, corresponding to the $(364.48 \pm 0.003_{\text{stat}} \pm 2.23_{\text{sys}})\,\text{fb}^{-1}$ luminosity collected on-resonance. The signal and background decay events are simulated using generic run-dependent MC15, incorporating the reconstruction efficiencies and acceptance effects of the detector. Therefore, we will refer to this as the reconstructed MC sample. The

continuum background events described in Sec. 4.2.3 are generated using the off-resonance sample with an integrated luminosity of $42\,\text{fb}^{-1}$.The generator or truth-level MC samples of B meson decays are generated using `EvtGen` [13]. This sample contains the true information of the simulated processes prior to the inclusion of detector effects. Subsequently, truth matching is performed by associating the reconstructed events with the corresponding true simulated events using the `PDG decay codes`. The effect of final-state radiation on charged particles is incorporated using `PHOTOS` [14] which simulates QED radiative corrections, primarily photons. `GEANT4` [15] is used to simulate the resolution effects when a particle interacts with the detector material. The generation of the MC samples, event reconstruction, and `PHOTOS` simulation of all the data sets are based on `release-08-01-10`, which is a full release of the open-source Belle II analysis software `basf2`[4]. In this analysis, the FEI calibration derived from $D^{(*)}\pi$ control samples [16] is used to ensure systematic robustness. Additionally, large parts of the reconstruction and modeling are done in collaborative work and are in accordance with the $B \to X_u \ell \nu$ branching fraction measurements [17] and the search for weak annihilation [18]. All plots produced in this analysis are using simulated and Asimov data.

CHAPTER 4

Reconstruction of inclusive $B \to X_c \ell \nu_\ell$ Decays

The data of the B meson that is collected by the detector needs to be reconstructed in order to perform the analysis on the decay of interest. This is accomplished using a technique known as *hadronic tagging*, which aims to identify the decay products of one B meson (B_{tag}) and thereby infer the decay of the other B meson (B_{sig}). A schematic diagram of this can be seen in Fig.4.1.

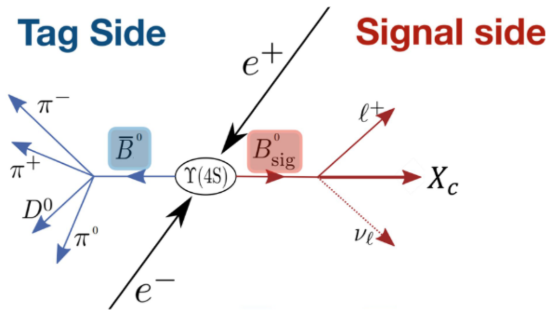

Figure 4.1: Schematic diagram showing the production of the two B mesons from e^+e^-; B_{tag} decays completely hadronically and B_{sig} decays into a charm hadronic system X_c, lepton and a neutrino. [19]

4.1 Tag Side Reconstruction

The reconstruction strategy begins by selecting one of the two B mesons as the tagged meson, denoted as B_{tag}, which is reconstructed exclusively hadronically, i.e., final states without leptons or neutrinos. This is performed using the multivariate *Full Event Interpretation* (FEI) algorithm in Fig. 4.2. A key advantage of this approach is that hadronic final states are fully observable in the detector. Since the four-momentum of the initial $\Upsilon(4S)$ system is precisely known, information about the signal-side B meson, B_{sig}, can be inferred from the reconstructed properties of B_{tag}. Thus, employing hadronic tagging using FEI, the full event kinetic information of the tag-side is obtained. The FEI algorithm starts from low-level detector information, such as reconstructed charged particle tracks, neutral energy deposits, and displaced vertices. These detector-level objects are first interpreted as stable final-state particles, including electrons, muons, charged pions and kaons, photons, and neutral hadrons. Subsequently, these particles are combined to

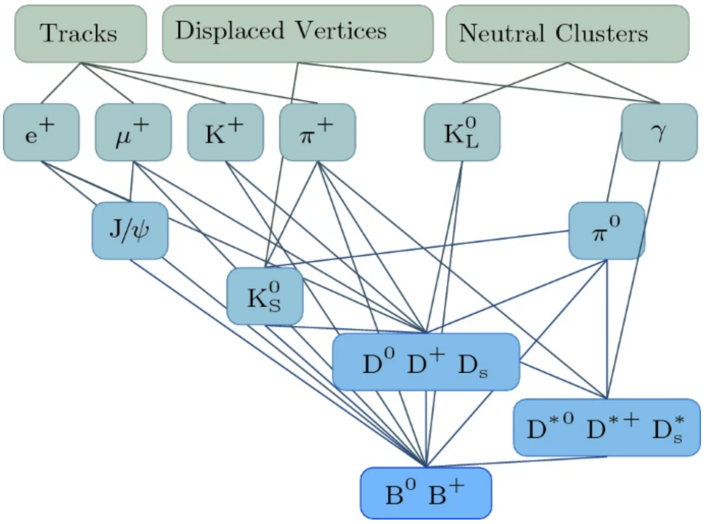

Figure 4.2: Schematic overview of the Full Event Interpretation [20]

form intermediate particles such as J/ψ, K_S^0, π^0, D, and D^* mesons. Through successive reconstruction steps, a complete hadronic decay chain of the tagged B meson is obtained. A detailed description of the FEI algorithm and its performance can be found in [21]. Furthermore, several selection criteria are applied to ensure the quality of the reconstructed B_{tag} candidates. Table 4.1 summarizes the selections used in this analysis.

Table 4.1: Selection criteria applied to the tag-side B_{tag} candidates.

Selection	Purpose
$-0.15 < \Delta E < 0.10$ GeV	$\Delta E = E_B^* - E_{\text{beam}}^*$ ensures that the reconstructed B energy is consistent with the beam energy in the center-of-mass frame.
$m_{\text{bc}} > 5.24$ GeV	$m_{\text{bc}} = \sqrt{{E_{\text{beam}}^*}^2 - {p_B^*}^2}$ retains the sideband region, which is useful for background studies and calibration.
$m_{\text{bc}} > 5.27$ GeV	A tighter requirement on m_{bc} improves the purity of correctly reconstructed B mesons in the final sample.
$\mathcal{P}_{\text{FEI}} > 0.01$	Removes poorly reconstructed tag candidates by requiring a minimum FEI signal probability.
Continuum suppression	Reduces jet-like background from $e^+e^- \to q\bar{q}$ events which mimic $B\bar{B}$ production.
Best candidate selection	Selects a single B_{tag} candidate per event to avoid multiple counting.
Off-resonance m_{bc} correction	Accounts for the center-of-mass energy difference between on-resonance and off-resonance data samples.

Once the tag-side decays have been identified, the signal-side B meson decay can be reconstructed using four-momentum conservation as discussed further in Sec. 4.2.

4.2 Signal Side Reconstruction

After reconstructing the tag-side B meson, the signal-side B_{sig} is reconstructed from the remaining particles in the event. The momentum of the signal-side B meson is determined using:

$$p_{B_{\text{sig}}} = p_{e^+e^-} - p_{B_{\text{tag}}}. \tag{4.1}$$

The signal-side selection requires the presence of a high-quality lepton (electron or muon) and the reconstruction of the hadronic system X_c from the remaining particles in the Rest of Event (ROE). Although the neutrino cannot be observed directly, its kinematic properties can be inferred from the known energies of the initial state. Table 4.2 summarizes the selections applied during the signal-side reconstruction in this analysis.

Table 4.2: Selection criteria applied to the signal-side candidates in B_{sig} decays.

Selection	**Purpose**
$p_\ell^{\text{CMS}} > 0.5$ GeV, $p_\ell^{\text{lab}} > 0.3$ GeV	Suppresses low-momentum background leptons and ensures reliable lepton reconstruction in both the lab and center-of-mass frames.
$\lvert\Delta z\rvert < 1$ cm, $\lvert\Delta r\rvert < 3$ cm	Ensures that the reconstructed lepton track originates from the interaction point, suppressing secondary tracks.
Electron ID: `BDT Score`> 0.9	Provides high-purity electron identification.
Muon ID: `LikelihoodID` > 0.9	Ensures high-purity muon identification.
Bremsstrahlung recovery (electrons)	Corrects for photon radiation emitted by electrons in the detector material.
`ProtonID` < 0.99	Reduces proton misidentification as leptons.
$m_{e^+e^-} < 0.05$ GeV veto	Removes photon conversion events where $\gamma \to e^+e^-$ pairs mimic signal electrons.
$3.043 < m_{\ell^+\ell^-} < 3.129$ GeV veto	Suppresses background from $J/\psi \to \ell^+\ell^-$ decays that produce real leptons unrelated to the semileptonic B decay signal

The hadronic system X_c is reconstructed from all remaining tracks and neutral clusters in the event that are not associated with the tag-side B candidate or the signal lepton. Additional quality requirements are applied to ensure that the reconstructed particles originate from the interaction point and satisfy detector acceptance criteria.

4.2.1 $B \to X_c \ell \nu$ Decay

The decay under consideration is the inclusive semileptonic decay is $B \to X_c \ell \nu$, where X_c denotes a hadronic final state containing a charm quark, ℓ represents a charged lepton (either an electron or a muon), and ν is the corresponding neutrino. The hadronic system X_c may consist of a variety of charm-containing particles, such as D mesons, D^* mesons, or other charmed hadrons. Since the decay is treated inclusively, the individual hadronic final states are not distinguished; instead, all possible configurations containing a charm quark are considered collectively. A Feynman diagram representation for this decay is shown in Fig. 4.3.

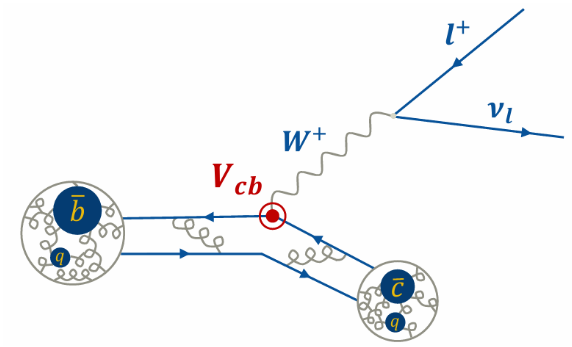

Figure 4.3: Feynman diagram of the $B \to X_c \ell \nu$ decay (time axis: horizontal). [22]

The B meson consists of a heavy anti-bottom quark $\bar{b}$ bound to a light quark q, whose flavor is not specified here. Due to the large mass of the $\bar{b}$ quark, the B meson decays rapidly, with a characteristic lifetime of order $\mathcal{O}(10^{-12}\,\text{s})$. At the quark level, the decay proceeds via the weak transition $\bar{b} \to \bar{c}$ mediated by the exchange of a virtual W boson. This intermediate boson subsequently decays into a charged lepton and its associated neutrino. These decay events are referred to as the *signal* events in the following analysis.

4.2.2 $B\bar{B}$ Background

The background processes can be broadly categorized into three main types:

1. **Secondary leptons:** Events in which the reconstructed lepton does not originate directly from the B meson decay. This category includes leptons produced in τ decays, but is dominated by contributions from semileptonic decays of charm hadrons, particularly D mesons.

2. **Misidentified leptons:** Events where a hadronic particle is reconstructed as a lepton. Such misidentification most frequently involves pions or kaons, for example those produced in tag-side decays or in processes such as $B \to DK/\pi$.

3. $B \to X_u \ell \nu$ **background:** Events in which the selected lepton arises from an inclusive $B \to X_u \ell \nu$ decay, including both resonant and non-resonant contributions.

These decays will be collectively referred to as *background* events in the subsequent analysis.

4.2.3 Continuum Background

The decay processes in which the e^+e^- annihilates to $q\bar{q}$ ($q = u, d, s, c$) events are commonly referred to as *continuum background*. This is evaluated using collision data collected at a reduced center-of-mass energy of $\sqrt{s} = 10.52\,\text{GeV}$. This dataset, known as the off-resonance sample, corresponds to an integrated luminosity of $42\,\text{fb}^{-1}$. As the data were recorded below the $\Upsilon(4S)$ resonance, the sample is dominated by non-resonant $e^+e^- \to q\bar{q}$ processes.

4.3 Kinematic Variables

The important kinematic variables of the $B \to X_c \ell \nu$ decay taken into consideration for this analysis are listed below:

1. M_X: Invaraint mass of the charm hadronic system X_c. This is calculated using the four-momenta of the other particles as discussed below. The invariant mass follows:

$$M_X^2 = p_X^2 \tag{4.2}$$

$$M_X = p_{B_{\text{sig}}} - p_\ell - p_\nu \tag{4.3}$$

2. q^2: Square of the four-momentum transfer or the invariant mass of the lepton-neutrino system. It is defined as

$$q^2 = \left(p_{B_{\text{sig}}} - p_X\right)^2 = (p_\ell + p_\nu)^2 \iff \quad p_\nu = p_{B_{\text{sig}}} - p_X - p_\ell \tag{4.4}$$

   where p (B_{sig}, X, ℓ, ν) represent the four-momenta of the B meson, hadronic system X_c, lepton ℓ and neutrino ν respectively. The four-momentum of the B meson can be inferred from the law of conservation of four-momentum given as:

$$p_{B_{\text{sig}}} = p_{e^+e^-} - p_{B_{\text{tag}}} \tag{4.5}$$

   The four-momentum of the tag-side is reconstructed from the *hadronic tagging* and the four-momentum of the $\Upsilon(4S)$ is known.

3. E_ℓ, p_ℓ: Energy and four-momentum of the lepton that is deposited and recorded from the detector. Further, E_ℓ^B (p_ℓ^B) and E_ℓ^{CMS} (p_ℓ^{CMS}) refers to the energy (momentum) in the rest frame of the B meson and the centre of mass system respectively.

4. $\cos\,\theta_\ell$: Cosine of the lepton helicity angle or the angle between the direction of the virtual W boson (in B meson rest frame) and the direction of the lepton (in W rest frame). It is defined as:

$$\cos\theta_l = \frac{\mathbf{p}_W^{B\text{-frame}} \cdot \mathbf{p}_l^{W\text{-frame}}}{\left\|\mathbf{p}_W^{B\text{-frame}}\right\| \cdot \left\|\mathbf{p}_l^{W\text{-frame}}\right\|} \tag{4.6}$$

CHAPTER 5

Resolution Studies

In this chapter, we focus on the visualization of the B_{tag} momentum in cylindrical coordinates and the study of the lepton helicity angle distribution. Furthermore, we investigate the impact of final-state radiation (FSR) photons on the $B \to X_c\, \ell\, \nu$ decay. In addition, this chapter introduces the concept of residual studies that is used to evaluate the resolution of the detector.

5.1 Data-MC agreement of tag-side B meson momentum $(p_{B_{tag}})$

Reconstructing the B_{tag} momentum is essential in $e^+e^- \to \Upsilon(4S) \to B\bar{B}$ events because the initial state four-momentum is precisely known. In the center-of-mass (CMS) frame, $p_{e^+e^-} = (\sqrt{s}, \vec{0})$ and since the $\Upsilon(4S)$ decays into a $B\bar{B}$ pair nearly at rest, full reconstruction of one B meson (the tag side) determines its four-momentum $p_{B_{\text{tag}}} = (E_{B_{\text{tag}}}, \vec{p}_{B_{\text{tag}}})$ which in turn can be used to completely reconstruct the signal-side B momentum through four-momentum conservation from Eq. 4.5.
Thus, any bias or mismodeling of the tag-side would directly propagate into the signal-side kinematics. Knowing $p_{B_{\text{sig}}}$ is particularly important for $B \to X_c \ell \nu$ decays because the neutrino is not directly detected and hence the four-momentum can be inferred from missing momentum as seen in Eq. 4.4.

This allows reconstruction of the key kinematic quantities such as those mentioned in Sec. 4.3. The three-momentum of the reconstructed B_{tag} meson can be expressed in cylindrical coordinates as $\vec{p}_{B_{\text{tag}}} = (p_T \cos\phi,\ p_T \sin\phi,\ p_z)^T$ where $p_T = \sqrt{p_x^2 + p_y^2}$ is the transverse momentum, $\phi = \tan^{-1}\left(\frac{p_y}{p_x}\right)$ is the azimuthal angle, and p_z is the longitudinal momentum along the beam axis. These observables with distinguished signal, background and continuum background events as discussed in Sec. 4.2.1, 4.2.2, 4.2.3 can be visualized in Fig. 5.1.

The distributions of the transverse momentum p_T, azimuthal angle ϕ, and longitudinal momentum p_z are well modeled in simulation and data, indicating that the FEI algorithm precisely reconstructed the tag-side B meson. The azimuthal angle, ϕ is expected to be symmetric and flat due to the rotational symmetry along the beam axis. Also, the boost that is produced along the beam axis due to the asymmetric e^+e^- collider can be well understood from the distribution of p_z.

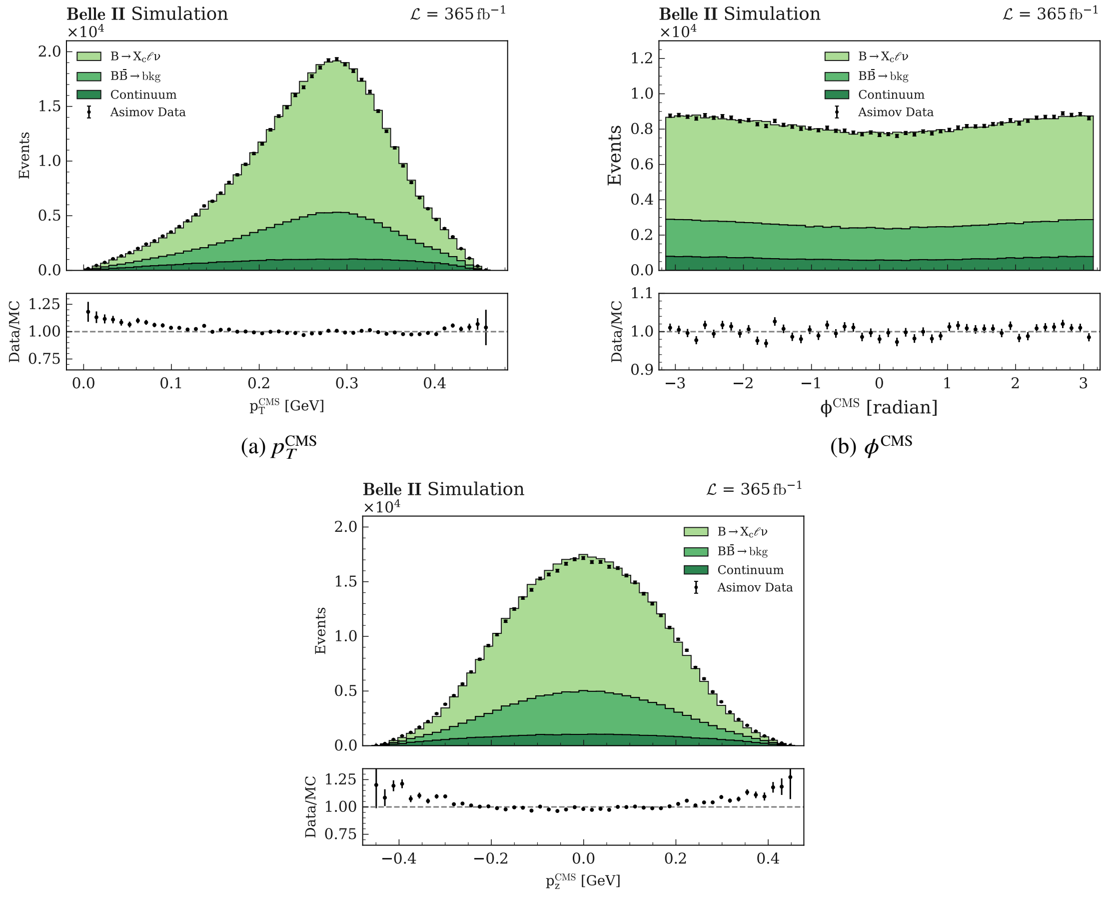

(a) p_T^{CMS} (b) ϕ^{CMS} (c) p_z^{CMS}

Figure 5.1: Distributions of the B_{tag} momentum components in the CMS frame: transverse momentum p_T, azimuthal angle ϕ, and longitudinal momentum p_z.

Precise determination of these quantities improves background suppression since incorrectly reconstructed events will not satisfy the overall four-momentum conservation. Therefore, accurate reconstruction of p_T, ϕ, and p_z of the B_{tag} is not merely a technical step, but it tests whether the reconstructed tag-side kinematics match expectations from simulation and therefore ensures proper modeling and reconstruction of the signal-side B meson.

5.2 Lepton Helicity Angle: cos θ_ℓ

The lepton helicity angle cos θ_ℓ is a fundamental angular observable in semileptonic B meson decays. It is defined as the cosine of the angle between the direction of the virtual W boson in the B meson rest frame and the direction of the charged lepton in the rest frame of the virtual W boson. In the B rest frame, the W boson and the X_c system recoil against each other and in the W rest frame, the lepton ℓ and the neutrino ν are emitted back-to-back. This can be visualized in Fig. 5.2.

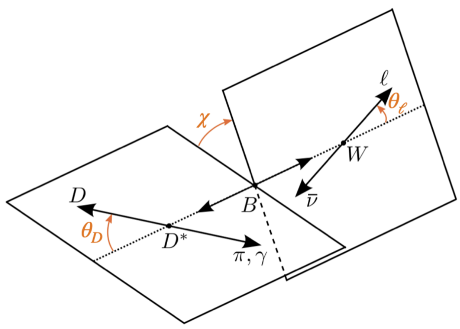

Figure 5.2: Helicity angle cos θ_ℓ

The momentum of the virtual W boson is defined as

$$p_W = p_{B_{\text{sig}}} - p_X, \tag{5.1}$$

where p_B^{sig} and p_X denotes the momentum of the signal-side and the hadronic system respectively. The momentum of the W boson is then boosted into the rest frame of the B meson to obtain the direction of flight of the W. Further, the charged lepton momentum is boosted into the center-of-mass frame of the virtual W boson. The cosine of the helicity angle is then constructed as a dot product of these momenta. Mathematically, this is expressed as

$$\cos\theta_\ell = \frac{\vec{p}_\ell^{\,W} \cdot \vec{p}_W^{\,B}}{|\vec{p}_\ell^{\,W}|\,|\vec{p}_W^{\,B}|}, \tag{5.2}$$

Fig. 5.3(a) shows the reconstructed distribution of the cos θ_ℓ for $B \to X_c \ell \nu$. It is also split into B meson decaying to D, D^*, D^{**} and the non-resonant gap channels in order to obtain a better understanding of the shape of cos θ_ℓ for exclusive decay channels. Each channel has a different angular structure because of the different isospins. It should also be noted that the shape of cos θ_ℓ for the $B \to D^{**}$ mode is a combined shape for $B \to D_0^*$, D_2^*, D_1 and $D_1^{'}$ decays and therefore involves mixing of isospin states.
Fig. 5.3(b) shows the generator level $cos\theta_\ell$ without any detector or reconstruction effects. If the combined $B \to X_c \ell \nu$ shape is compared in the two distributions, we see that the reconstructed distribution is smeared. This can be accounted for by the fact that the helicity angle involves missing momentum of the ν and the boosts into two frames.
Uncertainties in momentum magnitude, track direction, missing energy reconstruction, and boost determination propagate nonlinearly into cos θ_ℓ. The comparison between true and reconstructed distributions highlights the impact of smearing and motivates the use of migration matrices and unfolding techniques to recover the underlying physical angular distribution.

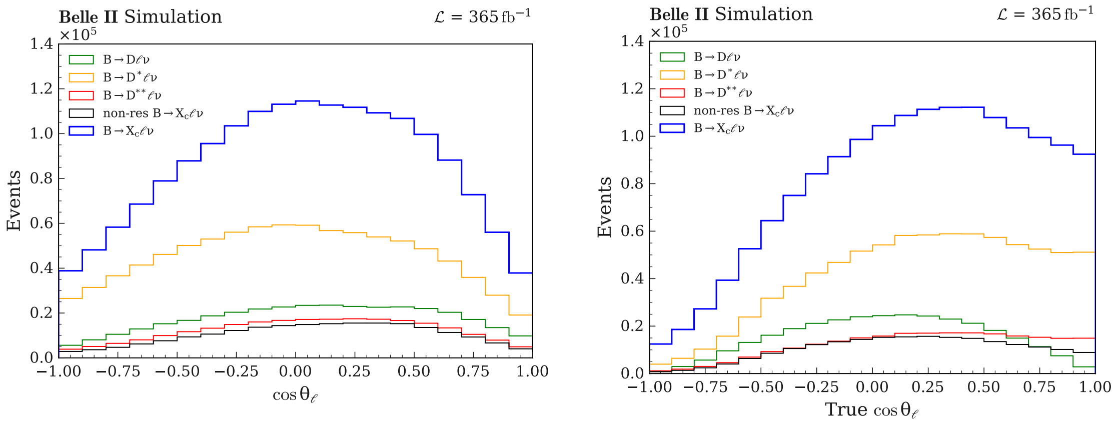

(a) Reconstructed cos θ_ℓ (b) Generated (truth-level) cos θ_ℓ

Figure 5.3: Cosine of the lepton helicity angle.

5.3 FSR Photons

FSR photons stands for *final-state radiation* photons that are emitted by charged particles in the final state of a reaction after the hard interaction or decay has taken place. Explaining based on this analysis, in semileptonic B decays of the form $B \to X_c\, \ell\, \nu$, FSR photons mainly refers to the QED photon emission from the outgoing lepton. The inclusive semileptonic decay in concern is given by Eq.1.1 where the main interaction produces X_c, ℓ and ν. Since the products include a charged lepton $\ell(e, \mu)$, QED allows $\ell \to \ell{+}\gamma$. Thus, the observed final state is $B \to X_c\, \ell\, \nu\, \gamma\, (\gamma\gamma\, \ldots)$. These photons are referred to as the FSR photons and can be visualized in Fig. 5.4. The PHOTOS[14] tool is used to generate and incorporate these QED radiative photons in the truth-level MC samples.

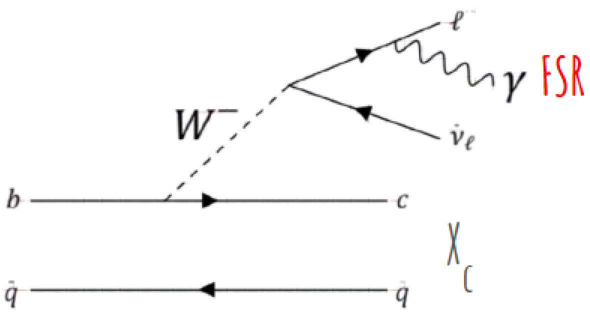

Figure 5.4: Feynman diagram showing the production of FSR photons in $B \to X_c\, \ell\, \nu$ semileptonic decays.

5.3.1 Effect of Final-State Radiation on E_ℓ and q^2

We study the impact of FSR photons on the lepton energy E_ℓ and the momentum transfer squared q^2, comparing the effects for electrons and muons. The probability for photon emission contains soft and collinear enhancements. In particular, the leading-logarithmic contribution behaves as

$$\delta_{\text{FSR}} \propto \alpha \ln\left(\frac{Q^2}{m_\ell^2}\right).$$

where α is the fine-structure constant, Q^2 is the characteristic hard scale of the process (of order m_B^2 or q^2), and m_ℓ is the lepton mass. The logarithmic term originates from collinear photon emission. The lepton mass acts as a regulator of the collinear divergence, such that lighter leptons allow radiation at smaller angles and therefore over a larger phase space. Since, $m_e \ll m_\mu$ the logarithm $\ln\left(\frac{Q^2}{m_e^2}\right)$ is significantly larger than $\ln\left(\frac{Q^2}{m_\mu^2}\right)$, leading to a much stronger FSR effect in the electron channel than in the muon channel. The distributions shown in Figs. 5.5 and 5.6 illustrate the comparison between simulations with `PHOTOS` (including FSR) and without `PHOTOS` (no FSR) for the electron (5.5(a) and 5.7) and muon (5.5(b) and 5.6(b)) channels.

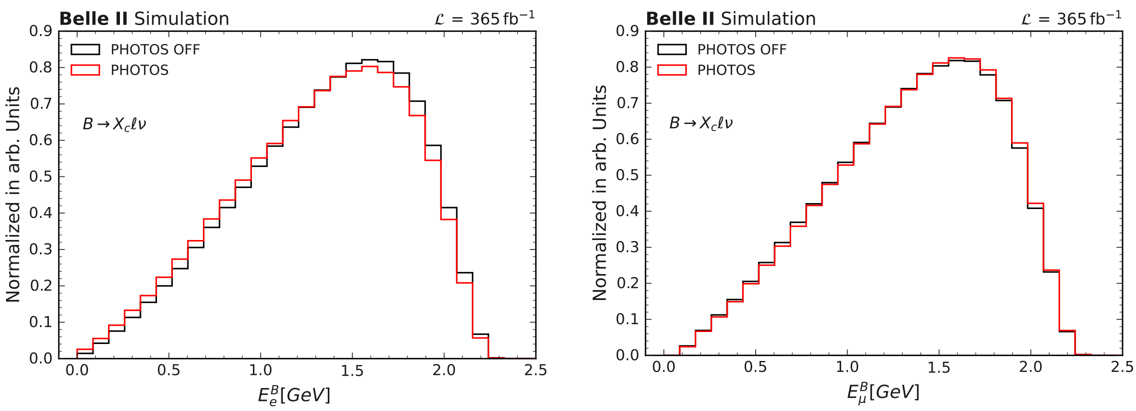

(a) E_e^B with (`PHOTOS`) and without (`PHOTOS` OFF) FSR photons.

(b) E_μ^B with (`PHOTOS`) and without (`PHOTOS` OFF) FSR photons.

Figure 5.5: Effect of final-state radiation photons on the electron and muon energy.

The effect of FSR on the lepton energy spectrum is shown in Fig. 5.5. For electrons, a visible distortion is observed when FSR is included (seen in red in Fig. 5.5). Since radiated photons carry away part of the lepton energy, the measured electron energy is shifted towards lower values. As a result, near the kinematic endpoint, the high E_ℓ region is depleted and hence the events migrate towards lower energy bins.
In contrast, the muon energy spectrum shows only a very small difference between the two configurations as the muon mass suppresses collinear radiation. The probability of significant photon emission is much smaller and therefore, the shape of the E_μ distribution remains largely unchanged. In the case of the momentum transfer squared $q^2 = (p_\ell + p_\nu)^2$, when FSR occurs, the measured lepton four-momentum is reduced $p_\ell^{\text{meas}} = p_\ell^{\text{true}} - p_\gamma$ leading to a systematically smaller reconstructed q^2. Consequently, events migrate from higher q^2 bins to lower q^2 bins, the high-q^2 tail is suppressed and the low-q^2 region is enhanced. This migration pattern is clearly visible in Fig. 5.6 for the electron channel, where the distribution containing the FSR photons (in red in Fig. 5.6) shows a relative enhancement at low q^2 and a depletion

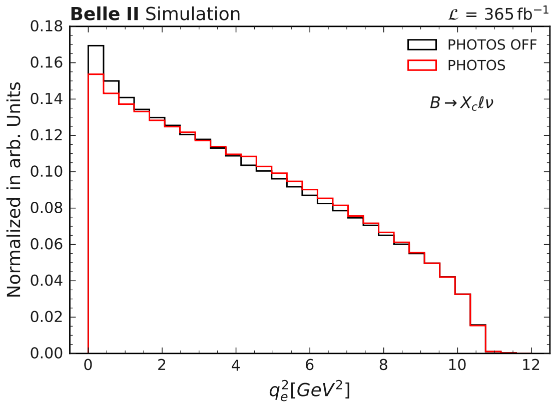

(a) q_e^2 with (PHOTOS) and without (PHOTOS OFF) FSR photons.

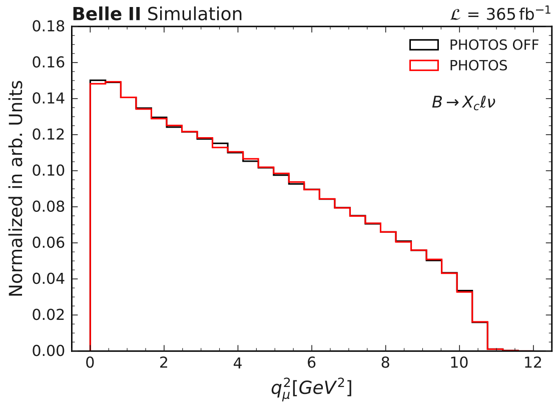

(b) q_μ^2 with (PHOTOS) and without (PHOTOS OFF) FSR photons.

Figure 5.6: Effect of final-state radiation photons on the momentum transfer squared for electrons and muons.

at high q^2. The effect is significantly smaller in the muon channel, again reflecting the reduced radiation probability due to the larger muon mass.

In summary, the lighter leptons can emit photons at much smaller angles relative to their direction, increasing the available phase space for implying a larger radiative correction. Therefore, final-state radiation introduces sizable distortions in the electron channel, while its impact on muons remains comparatively small due to the larger lepton mass.

5.4 Distributions of Δq^2 and ΔE_ℓ^B

To quantify the detector resolution and understand the smearing between truth-level and reconstructed kinematics, the differences between true and reconstructed observables are studied. These resolution distributions provide direct insight into detector performance and are essential inputs for migration-matrix construction and unfolding. We define the residuals as

$$\Delta q^2 = q^2_{\text{true}} - q^2_{\text{reco}} \tag{5.3}$$

$$\Delta E_\ell^B = E^B_{\ell,\text{true}} - E^B_{\ell,\text{reco}}. \tag{5.4}$$

If the reconstruction were perfect, both distributions would be delta functions centered at zero. In practice, detector resolution, reconstruction uncertainties, and radiative effects broaden these distributions and introduce biases.

The mean of a residual distribution $\mu = \langle x_{\text{true}} - x_{\text{reco}} \rangle$ quantifies systematic bias. A non-zero mean indicates that the reconstruction systematically over or underestimates the observable. The root mean square RMS $= \sqrt{\langle (\Delta x)^2 \rangle}$ quantifies the overall resolution. It measures the typical size of fluctuations around the mean and includes both Gaussian core resolution and non-Gaussian tails. Together, the mean and RMS provide a compact summary of reconstruction bias, detector resolution and sensitivity to radiative and missing-energy effects.

Fig. 5.7(a) shows the distribution of Δq^2 for the electron and muon channels. The distributions are

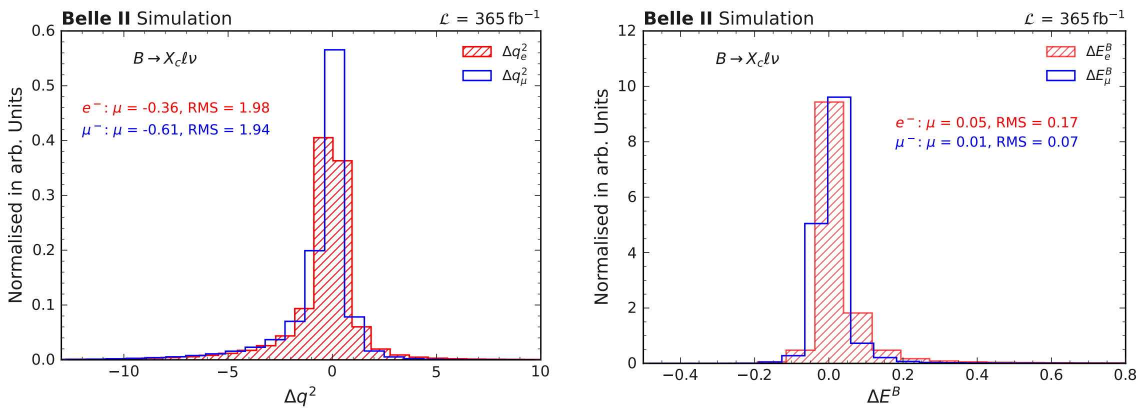

(a) Δq^2 (b) ΔE_ℓ^B

Figure 5.7: Distributions of Δq^2 and ΔE_ℓ^B. e channels are indicated in red and μ channels are indicated in blue.

centered near zero but exhibit noticeable widths and non-Gaussian tails. The mean values are: $\mu_e \approx -0.36$ GeV^2 and $\mu_\mu \approx -0.61$ GeV^2. The mean quantifies the **bias** of the reconstruction. A non-zero mean indicates a systematic shift between reconstructed and true values. The negative mean observed here implies that, on average, the reconstructed value of q^2 is slightly larger than the true value. The RMS values are RMS(e) $\approx$ 1.98 GeV^2 and RMS(μ) $\approx$ 1.94 GeV^2. The RMS measures the **resolution width** of the distribution and characterizes the typical magnitude of reconstruction fluctuations. The relatively large RMS reflects the compounded uncertainties from the lepton momentum resolution and the neutrino momentum reconstruction.

Fig. 5.7(b) shows the corresponding distributions for ΔE_ℓ^B. The means are: $\mu_e \approx 0.05$ GeV and $\mu_\mu \approx 0.01$ GeV. These values are close to zero, indicating negligible bias in the reconstruction of E_ℓ^B. The RMS values are RMS(e) $\approx$ 0.17 GeV and RMS(μ) $\approx$ 0.07 GeV. The smaller RMS compared to Δq^2 reflects the superior resolution of direct lepton energy reconstruction relative to quantities involving missing energy.

The lower RMS value of the muon channel for the Δq^2 and ΔE_ℓ^B confirms significantly better resolution, consistent with reduced bremsstrahlung and more stable momentum measurement. The larger RMS in the electron channel arises from radiative energy loss and imperfect photon recovery.

CHAPTER 6

Inclusive Branching Ratio Measurement

This chapter presents the construction of migration matrices for the kinematic variables and includes information on the fitting model that incorporates the templates of the signal, background and continuum background events and calculates the signal yields. The efficiency corrections of the detector with respect to the lepton momentum p_ℓ, momentum-transfer squared, q^2 and the lepton helicity angle, cos θ_ℓ are calculated, and are used in the complete unfolding procedure along with the migration matrices of the kinematic variables in order to obtain the truth-level kinematic spectrum. Further, this chapter includes the calculation of the absolute branching ratios for the $B \to X_c \ell \nu$ decay for the electron and muon channels.

6.1 Migration Matrices

In this analysis, we consider a simulated MC sample that incorporates the reconstructed efficiencies and the acceptance effects of the detector, referred to as the "reconstructed" sample, and a "generator" or "truth-level" sample containing true information before the application of detector effects. The migration matrix (also called the response matrix) provides a quantitative description of how events migrate from their true kinematic bin to a reconstructed bin. It is essential in detector correction procedures, particularly in unfolding, where measured distributions are corrected back to particle-level or truth-level quantities.

Let x denote a kinematic observable (q^2, E_ℓ, p_ℓ, cos θ_ℓ). Each observable is discretized into bins at both, the truth level (bins indexed by j) and the reconstructed level (bins indexed by i). For a given event in the MC simulation, both the true value x^{true} and the reconstructed value x^{reco} are known. Each event can therefore be uniquely assigned to:

- a truth bin j, determined by x^{true}, and
- a reconstructed bin i, determined by x^{reco}.

The migration matrix M is defined as the conditional probability

$$M_{ij} = P(\text{reconstructed in bin } i \mid \text{true in bin } j). \tag{6.1}$$

Thus, for a fixed truth bin j, the matrix elements M_{ij} quantify the probability that an event generated in bin j is reconstructed in bin i. Each column j of the matrix therefore has a clear physical meaning corresponding to a fixed true kinematic region describing how events originating in that truth bin are distributed across reconstructed bins. In the ideal limit of perfect detector resolution and efficiency, the migration matrix would be reduce to the identity matrix, $M_{ij} = \delta_{ij}$.

6.1.1 Interpretation of the E_ℓ^B, p_ℓ^B and q^2 migration matrices

The migration matrices for the moments E_ℓ^B, p_ℓ^B and q^2 in the electron and muon channels are visualized in Figs. 6.2, 6.1 and 6.3.

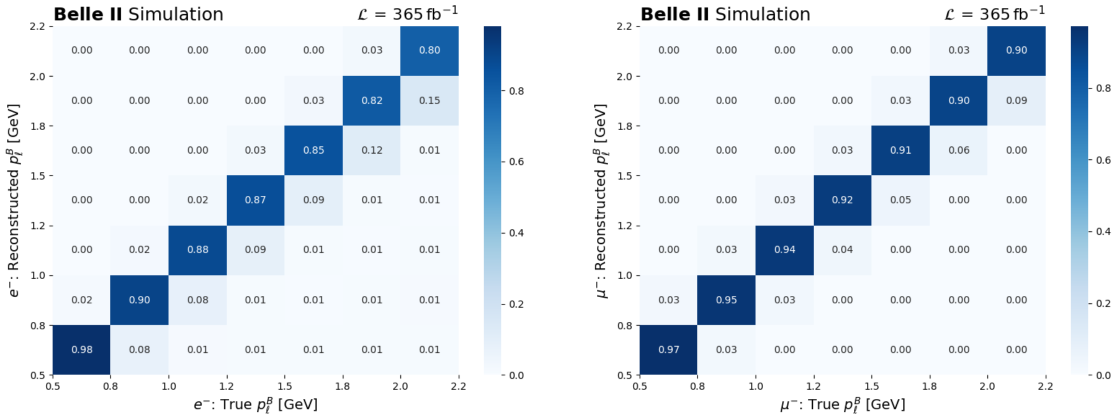

(a) p_e^B (b) p_μ^B

Figure 6.1: Migration matrices for p_ℓ^B separated into electron mode (left) and muon mode (right).

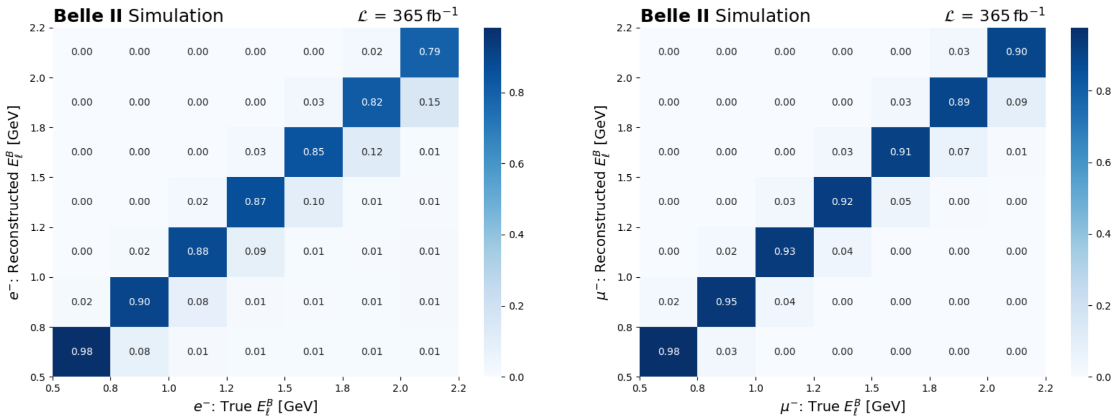

(a) E_e^B (b) E_μ^B

Figure 6.2: Migration matrices for E_ℓ^B separated into electron mode (left) and muon mode (right).

The migration matrices for the lepton energy and momentum in the B rest frame, E_ℓ^B (Fig. 6.2) and p_ℓ^B (Fig. 6.1) are highly diagonal for both channels with large diagonal probabilities typically close to unity in the lower and intermediate bins. This indicates excellent resolution for E_ℓ^B and p_ℓ^B in the chosen binning and implies that only a small fraction of events migrate out of their truth bin. At higher E_ℓ^B and p_ℓ^B, the diagonal probabilities decrease slightly, and the migration into adjacent bins becomes more visible. This reflects the growing impact of resolution effects and non-Gaussian tails in the reconstruction. Since the p_ℓ^B is obtained after boosting the lepton four-momentum into the reconstructed B rest frame, uncertainties in the B meson momentum reconstruction also propagate into this observable, contributing to bin migration. The muon channel exhibits a slightly tighter diagonal structure than the electron channel, consistent with better muon momentum reconstruction and reduced radiative energy-loss effects. The electron channel shows comparatively enhanced off-diagonal contributions, consistent with bremsstrahlung-induced tails resulting in a shift of the reconstructed lepton energy toward lower values, as a fraction of the lepton's energy is carried away by radiated photons.

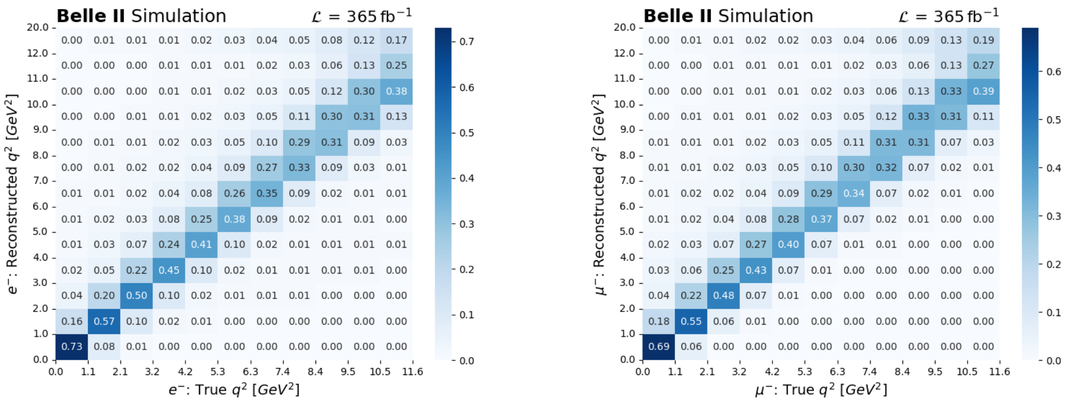

(a) q_e^2 (b) q_μ^2

Figure 6.3: Migration matrices for q_ℓ^2 separated into electron mode (left) and muon mode (right).

The q^2 migration matrices (Fig. 6.3) exhibit dominant diagonal elements in both lepton channels, indicating that the reconstruction preserves the q^2 bin assignment for the majority of events. The predominant construction of the off-diagonal elements in neighboring bins implies that the detector smearing leads mainly to local bin-to-bin migrations rather than long-range distortions. As seen in Fig. 6.3, at the truth level, the observable q^2 is strictly bounded by the kinematics of the decay with an upper limit of approximately $q^2_{\mathrm{max}} \approx 11.6\ \mathrm{GeV}^2$ for the decay under study. This endpoint arises from energy–momentum conservation. In contrast, the reconstructed q^2 distribution extends beyond the kinematic endpoint. This is a direct consequence of finite detector resolution and uncertainties in the reconstruction of the neutrino momentum. These effects smear the measured four-momenta and can yield reconstructed values of q^2 that exceed the physically allowed region. Including these overflow regions is essential to correctly model bin-to-bin migration in the unfolding procedure.

A difference is observed between the electron and muon channels. The electron matrix shows a broader diagonal band and enhanced off-diagonal contributions compared to the muon matrix. In addition, the electron response exhibits a migration pattern consistent with a tendency toward lower reconstructed q^2 values. This behavior arises primarily from bremsstrahlung energy loss in detector material. If the radiated energy is not fully recovered, the reconstructed electron momentum is biased low, which propagates into q^2 and results in migration toward smaller reconstructed values. Muons, being minimally ionizing particles, undergo negligible bremsstrahlung and therefore show a narrower response with reduced migration.

The migration matrix therefore provides a complete probabilistic description of how detector effects and efficiencies transform the true spectrum into the measured one, and it forms the fundamental input for unfolding procedures correcting the measured spectra back to the truth-level spectrum.

6.1.2 Interpretation of the cos θ_ℓ Migration Matrix

The migration matrix for the angular observable cos , θ_ℓ in Fig. 6.4 exhibits significantly stronger smearing compared to observables such as q^2, E_ℓ^B and p_ℓ^B. This behavior reflects the intrinsic sensitivity of angular variables to momentum resolution, boost reconstruction, and acceptance effects.

The observable cos θ_ℓ is defined in Sec. 4.3. Its evaluation depends on two different Lorentz boosts and the measurement of $p_{B_{\text{sig}}}$, p_{X_c} and p_ℓ. The uncertainties in any of these ingredients propagate nonlinearly into cos θ_ℓ. In contrast to energy-like observables, which depend primarily on the magnitude of the momentum, cos θ_ℓ depends on the full vector orientation, making it particularly sensitive to small angular mismeasurements. Modest uncertainties in track direction or in the boost to the virtual frame of the W boson can induce sizable shifts in the reconstructed angular value, leading to enhanced bin-to-bin migration.

In addition, cos θ_ℓ is a bounded observable, $-1 \leq \cos\theta_\ell \leq 1$, which introduces edge effects near the kinematic boundaries. Small reconstruction uncertainties close to cos $\theta_\ell = \pm 1$ can result in relatively large bin migrations toward interior bins, reducing diagonal dominance in the response matrix.

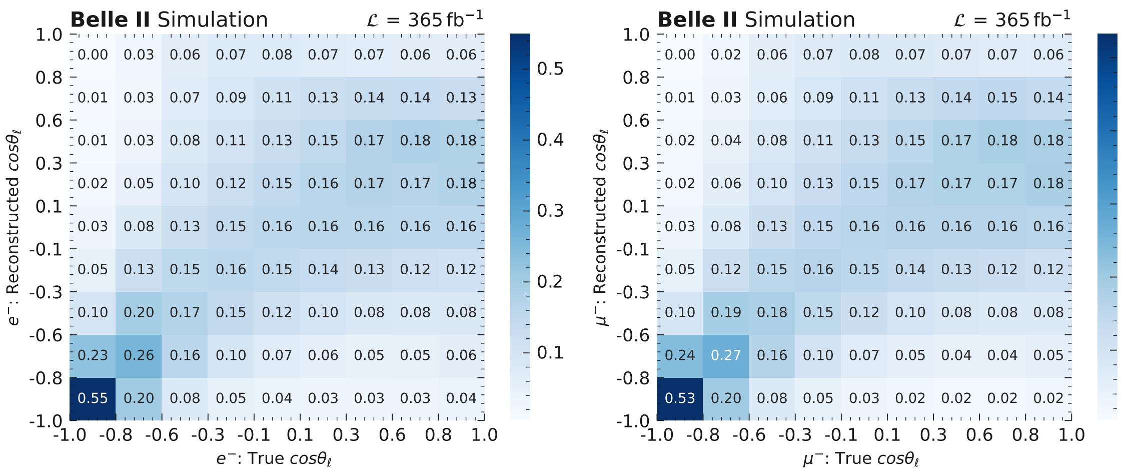

(a) $cos\ \theta_e$ (b) $cos\ \theta_\mu$

Figure 6.4: Migration matrices for $cos\ \theta_\ell$

For the electron channel, bremsstrahlung further enhances smearing effects. Photon emission modifies both the magnitude and effective direction of the reconstructed momentum, amplifying angular distortions. The muon channel typically exhibits a considerably improved resolution due to the reduced impact of radiative energy loss, though it remains sensitive to boost reconstruction effects. Overall, the cos θ_ℓ migration matrix shows weaker diagonal dominance and a broader off-diagonal structure compared to the q^2, E_ℓ^B and p_ℓ^B moments reflecting the compounded sensitivity of angular observables to detector resolution and event kinematics.

6.2 Signal Yields Extraction

The extraction of the signal yield is performed through a fit to the invariant mass of the hadronic system, M_X. The data are divided into fine bins of the kinematic variable p_ℓ^B, spanning the range $0.3 \le p_\ell^B \le 2.3$ GeV with a bin width of 0.1 GeV. No extrapolation is performed to $p_\ell^B = 0$ GeV.

Within each p_ℓ^B bin, the corresponding M_X spectrum is further partitioned into three coarse intervals, defined as [0, 1.8], [1.8, 2.7], and [2.7, 4.0] GeV. A binned maximum-likelihood fit is then carried out in each bin using a statistical model implemented with the `pyhf` framework. The model includes distinct template components for the signal process $B \to X_c \ell \nu$, the $B\bar{B}$ background, and the continuum background, as described in Sec. 4.2.1, Sec. 4.2.2, and Sec. 4.2.3, respectively.

The construction of the statistical model, the treatment of systematic uncertainties, and the execution of the fitting workflow are managed using the `cabinetry` framework. When fitting the M_X distributions, systematic uncertainties arising from sources such as branching fractions, form factors, particle identification, and tracking efficiencies are incorporated as nuisance parameters in the likelihood model. Detailed study and examination of each systematic uncertainty contribution as nuisance parameters can be found in Sec. 7.

The signal yields are determined from the fit and serve as the basis for unfolding and the extraction of differential branching fractions as well as the total branching fraction as discussed in Sec. 6.5. The fits are performed independently for the electron and muon channels. Fig. 6.5 and Fig. 6.6 show the post-fit results respectively for each p_e^B bin in [0.3, 2.3] GeV fitted in the three coarse bins of M_X. Similarly, Fig. 6.7 and Fig. 6.8 show the post-fit results respectively for each p_μ^B bin. The yields are obtained separately for the B^0_{tag} and B^+_{tag} but are combined later in the analysis when used in the consequent measurements.

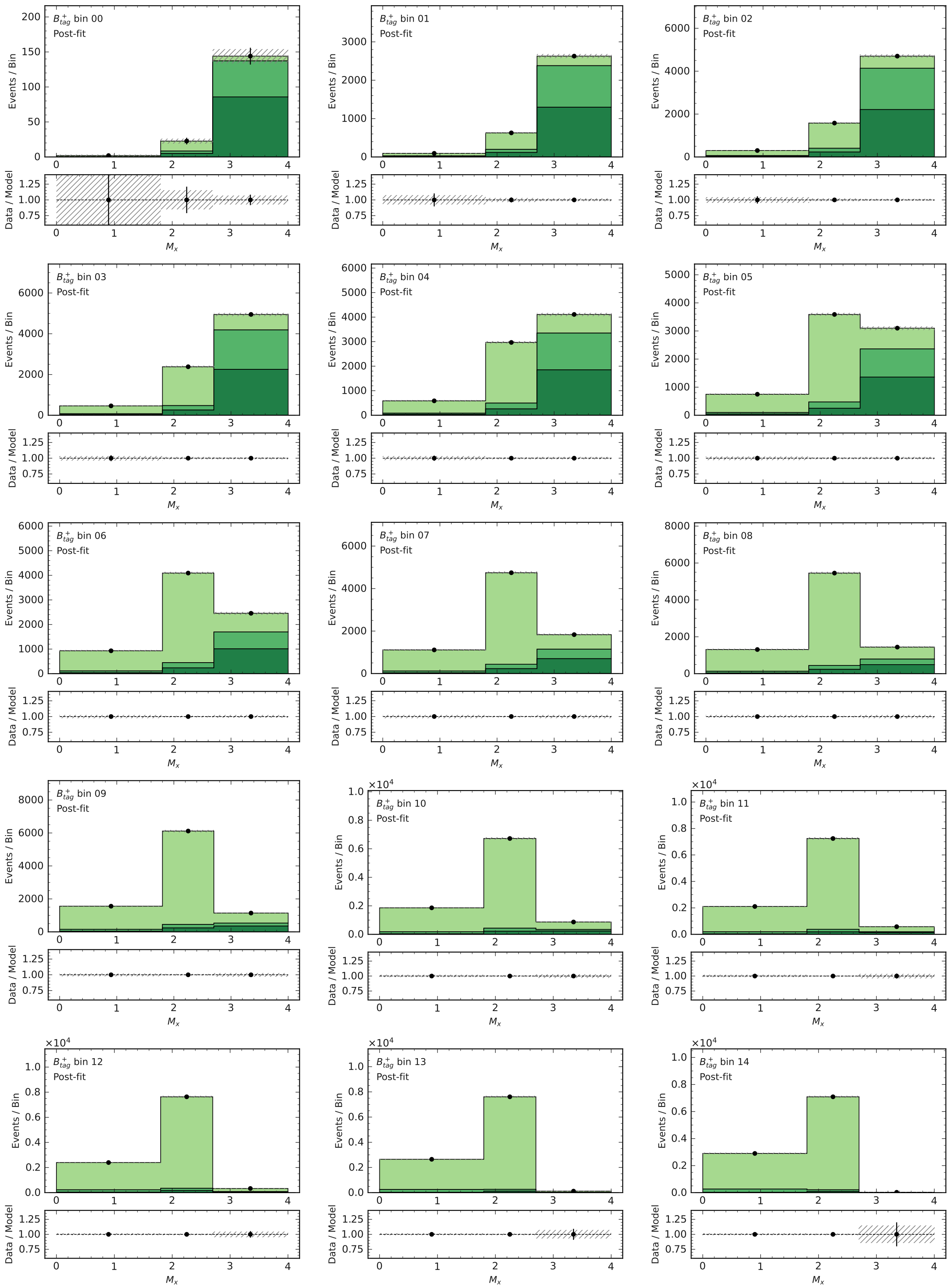

B^+_{tag} bin 00
Post-fit
B^+_{tag} bin 01
Post-fit
B^+_{tag} bin 02
Post-fit
B^+_{tag} bin 03
Post-fit
B^+_{tag} bin 04
Post-fit
B^+_{tag} bin 05
Post-fit
B^+_{tag} bin 06
Post-fit
B^+_{tag} bin 07
Post-fit
B^+_{tag} bin 08
Post-fit
B^+_{tag} bin 09
Post-fit
B^+_{tag} bin 10
Post-fit
B^+_{tag} bin 11
Post-fit
B^+_{tag} bin 12
Post-fit
B^+_{tag} bin 13
Post-fit
B^+_{tag} bin 14
Post-fit
Events / Bin
Data / Model
M_x
$\times 10^4$

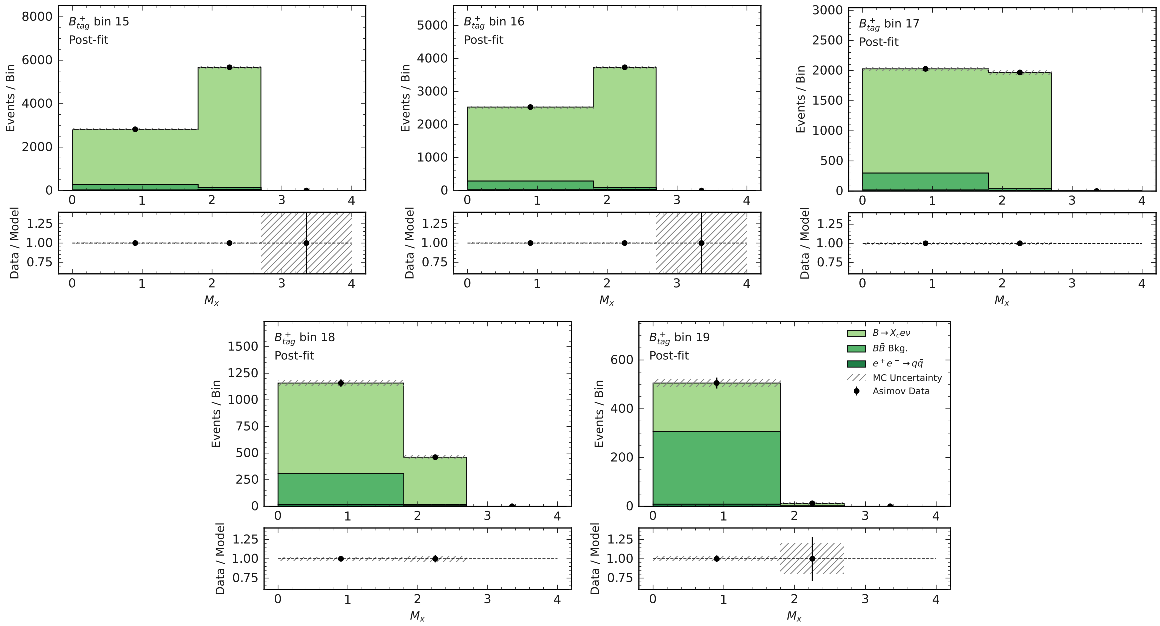

Figure 6.5: Post-fit distributions of the fine p_e bins within $0.3 \le p_e \le 2.3$ GeV in 0.1GeV bins each for B^+, obtained from fits performed in three coarse M_X intervals: $[0, 1.8, 2.7, 4.0]$ GeV. In the plot, `bin 00` refers to the p_e interval $[0.3, 0.4]$ GeV, `bin 01` refers to the p_e interval $[0.4, 0.5]$, GeV and so on.

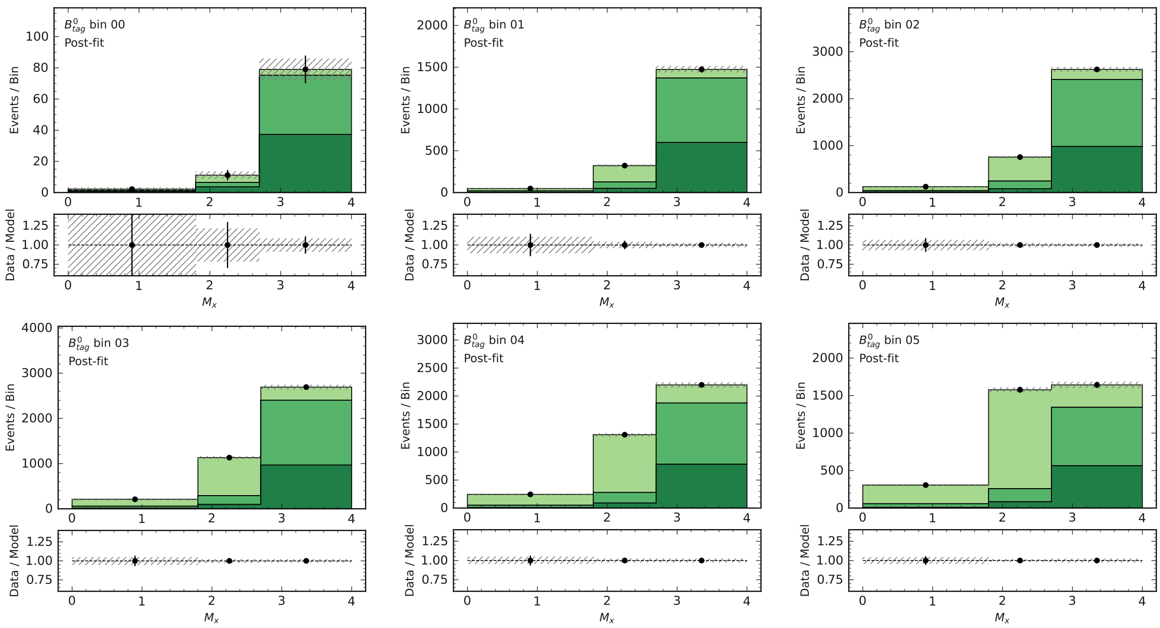

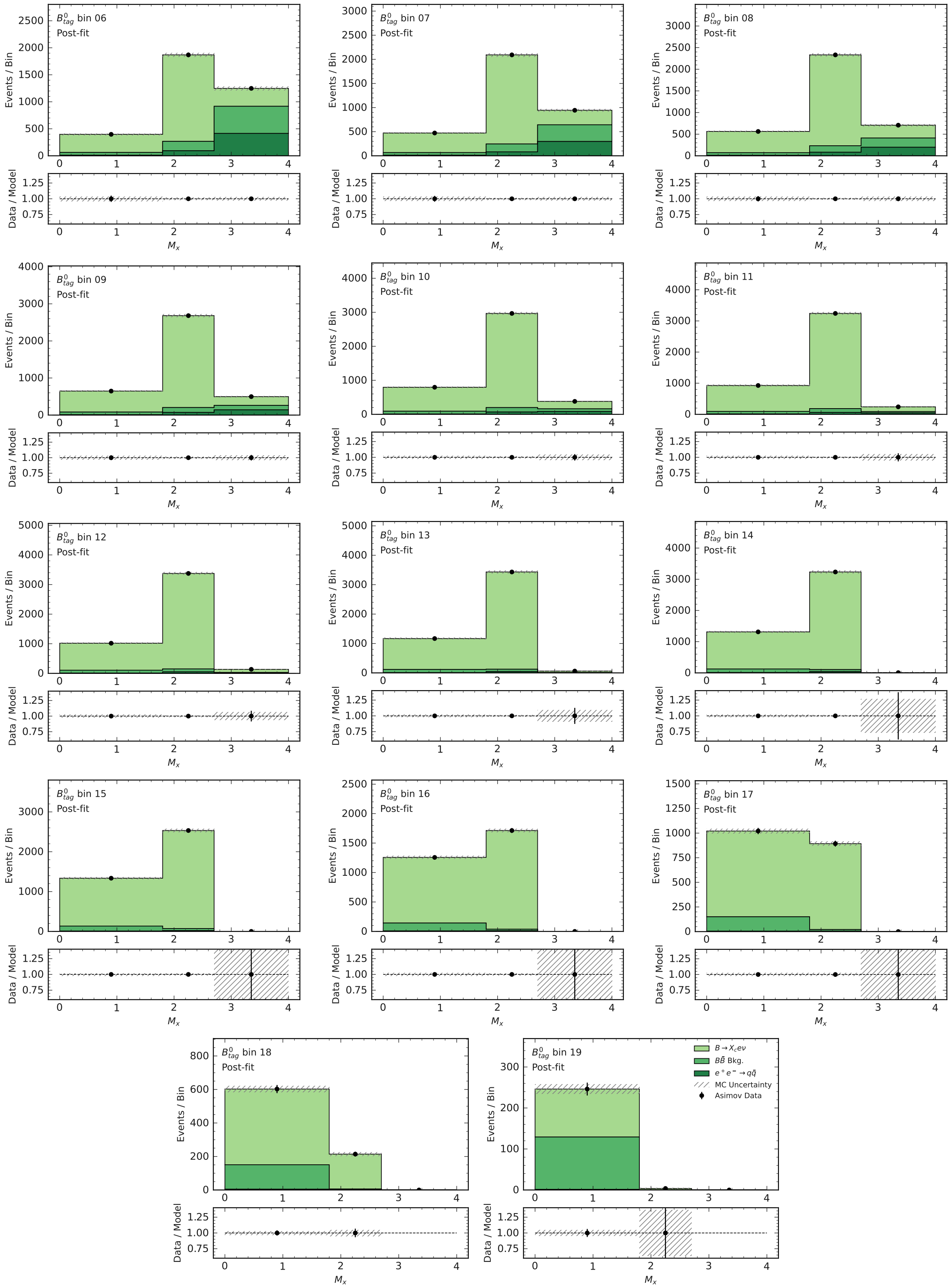

Figure 6.6: Post-fit distributions of the fine p_e bins within $0.3 \leq p_e \leq 2.3$ GeV in 0.1GeV bins each for B^0, obtained from fits performed in three coarse M_X intervals: $[0, 1.8, 2.7, 4.0]$ GeV. In the plot, `bin 00` refers to the p_e interval $[0.3, 0.4]$ GeV, `bin 01` refers to the p_e interval $[0.4, 0.5]$, GeV and so on.

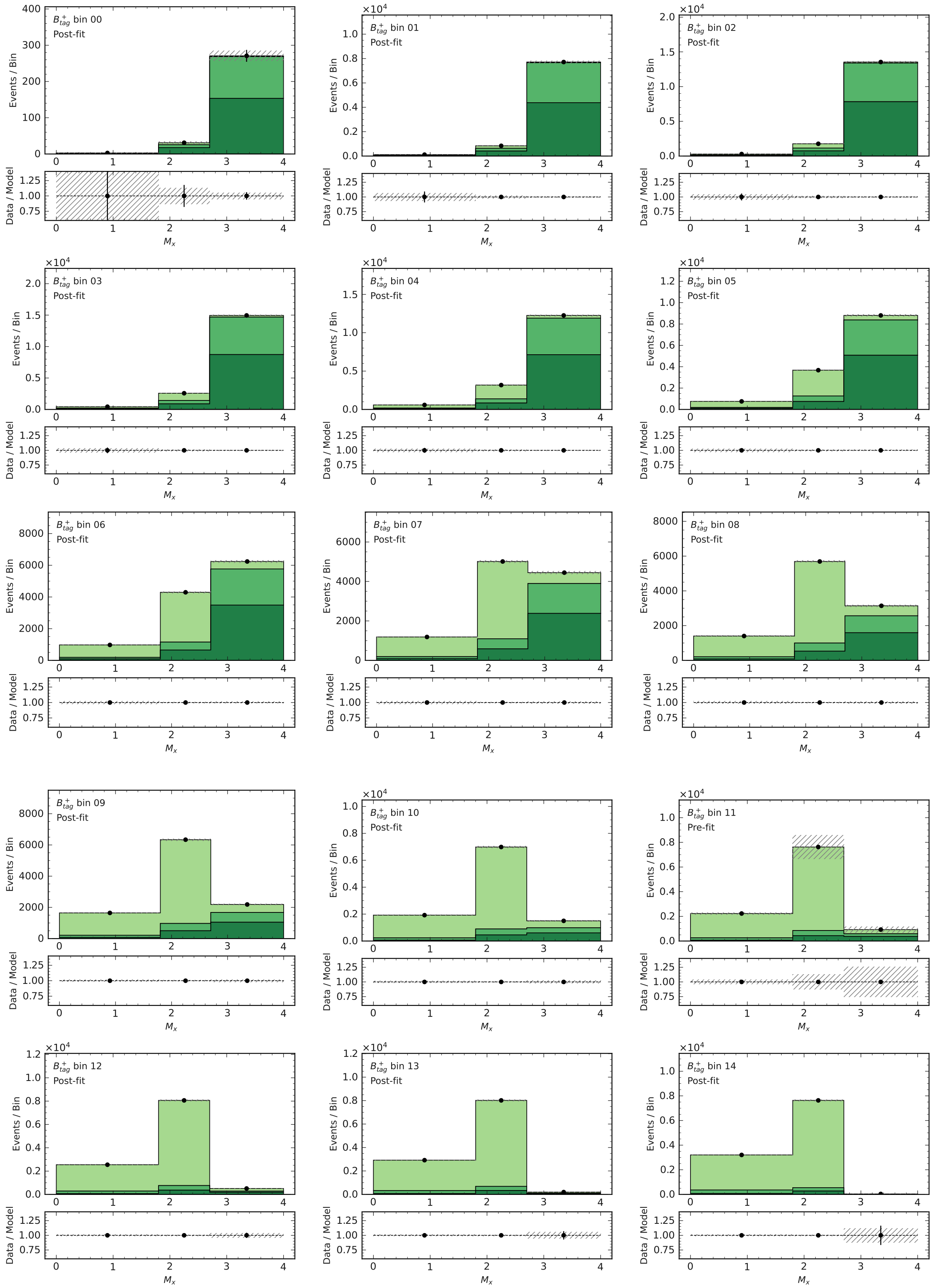
B^+_{tag} bin 00
Post-fit
B^+_{tag} bin 01
Post-fit
B^+_{tag} bin 02
Post-fit
B^+_{tag} bin 03
Post-fit
B^+_{tag} bin 04
Post-fit
B^+_{tag} bin 05
Post-fit
B^+_{tag} bin 06
Post-fit
B^+_{tag} bin 07
Post-fit
B^+_{tag} bin 08
Post-fit
B^+_{tag} bin 09
Post-fit
B^+_{tag} bin 10
Post-fit
B^+_{tag} bin 11
Pre-fit
B^+_{tag} bin 12
Post-fit
B^+_{tag} bin 13
Post-fit
B^+_{tag} bin 14
Post-fit
Events / Bin
Data / Model
M_x

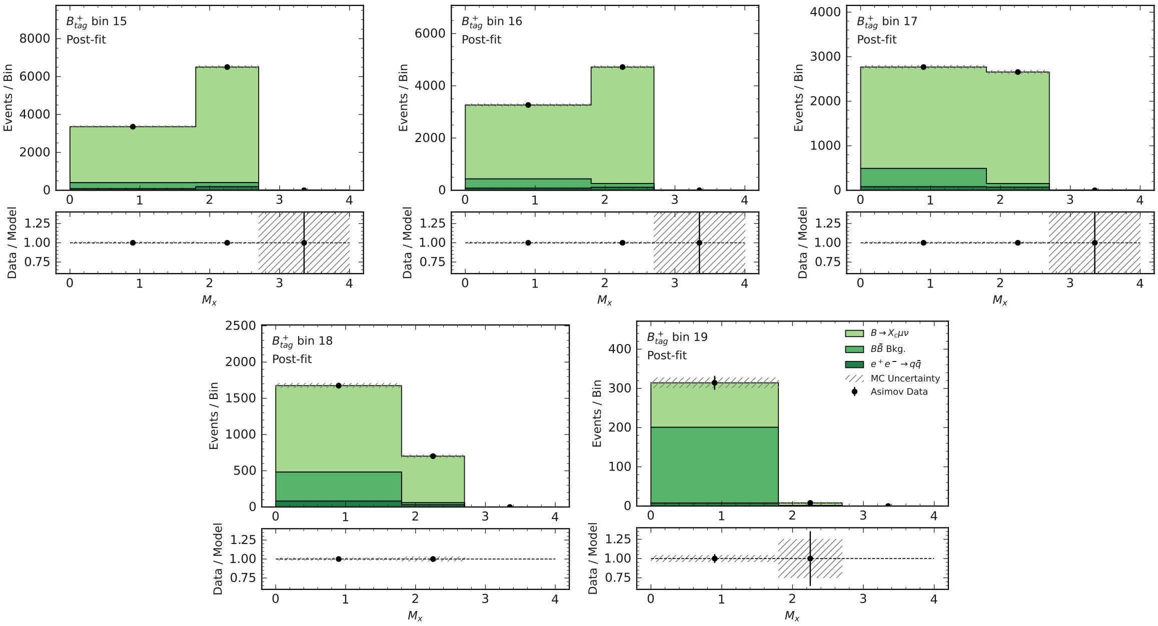

Figure 6.7: Post-fit distributions of the fine p_μ bins within $0.3 \leq p_\mu \leq 2.3$ GeV in 0.1GeV bins each for B^+, obtained from fits performed in three coarse M_X intervals: $[0, 1.8, 2.7, 4.0]$ GeV. In the plot, `bin 00` refers to the p_μ interval $[0.3, 0.4]$ GeV, `bin 01` refers to the p_μ interval $[0.4, 0.5]$, GeV and so on.

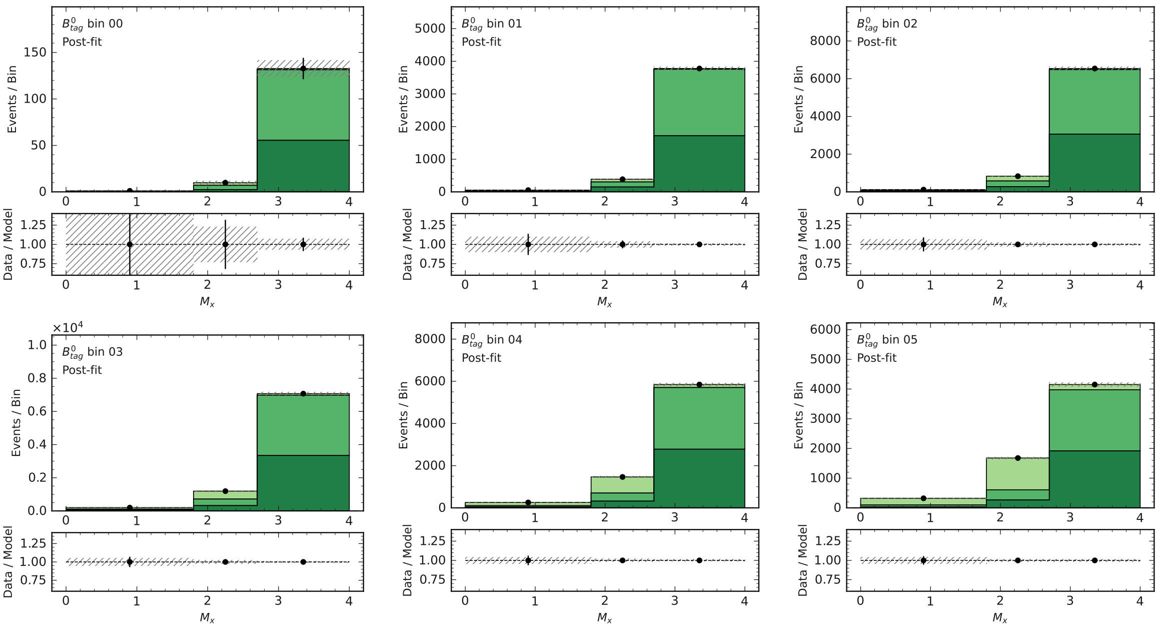

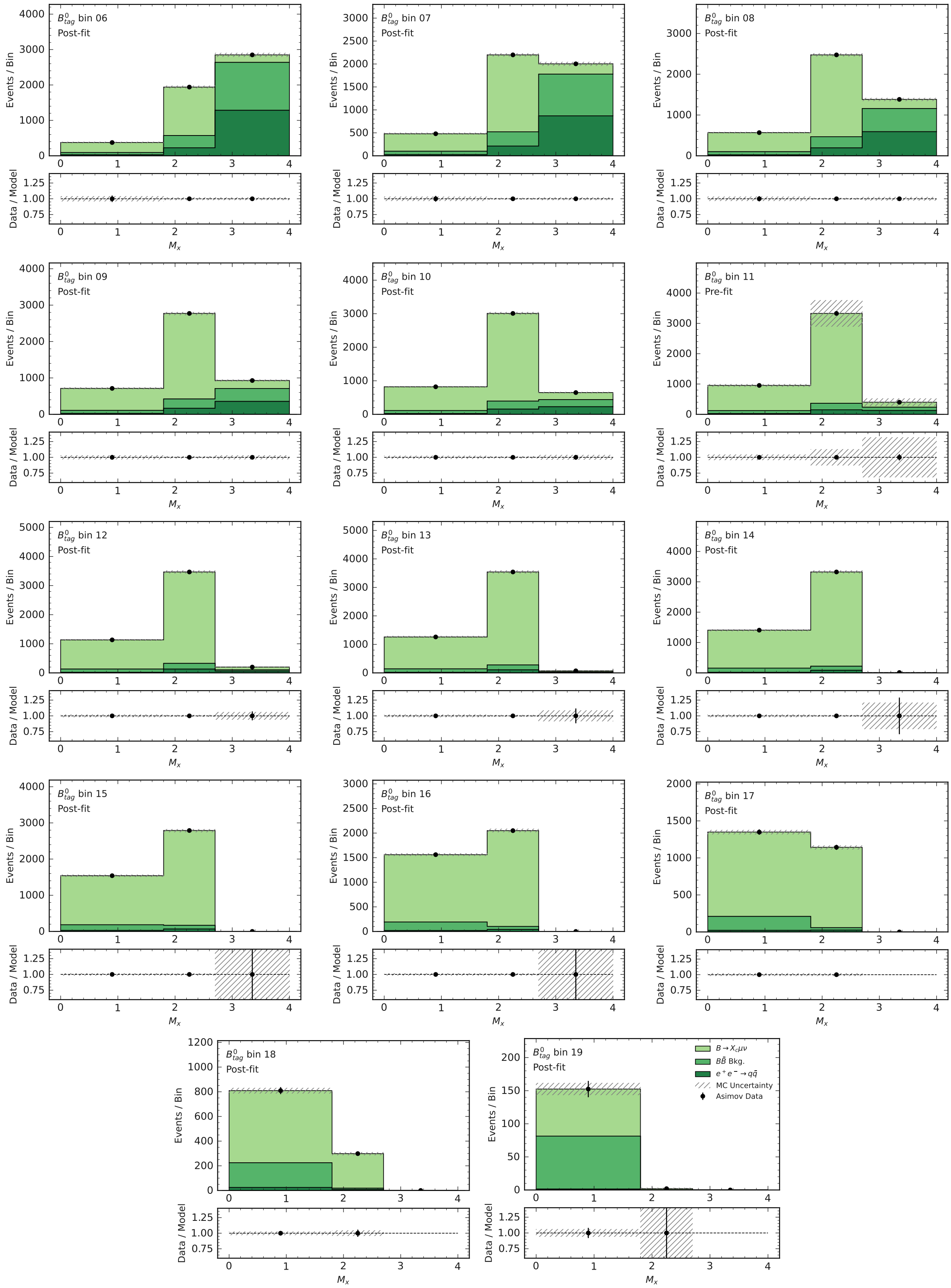

Figure 6.8: Post-fit distributions of the fine p_μ bins within $0.3 \leq p_\mu \leq 2.3$ GeV in 0.1GeV bins each for B^0, obtained from fits performed in three coarse M_X intervals: $[0, 1.8, 2.7, 4.0]$ GeV. In the plot, `bin 00` refers to the p_μ interval $[0.3, 0.4]$ GeV, `bin 01` refers to the p_μ interval $[0.4, 0.5]$, GeV and so on.

The use of coarse M_X intervals ensures the stability of the binned maximum-likelihood fit, particularly in the presence of multiple nuisance parameters associated with the systematic uncertainties. Signal and background events have different shapes in the hadronic mass M_X. Performing the fit in M_X bins provides strong signal-background discrimination and allows a good separation of the different charm final states while retaining sufficient statistics. The fit is carried out independently in bins of p_ℓ^B to properly account for the correlation between M_X and p_ℓ^B and to extract the signal yields in each momentum region. This strategy enables a robust determination of the differential branching fractions as a function of p_ℓ^B, as well as their subsequent integration to obtain the total branching fraction as seen in Sec. 6.5.

In addition to the extraction of signal yields as a function of the lepton momentum p_ℓ^B, the analysis is extended to the kinematic variables given by the momentum transfer squared q^2 and the helicity angle of the charged lepton $\cos\theta_\ell$. The signal yields in these variables are obtained using a similar fitting strategy by performing binned maximum-likelihood fits to the hadronic mass distribution M_X in each kinematic bin.

The q^2 spectrum is divided into twelve uniform bins spanning the range $0 \leq q^2 \leq 12\ \mathrm{GeV}^2$, with a bin width of $1\ \mathrm{GeV}^2$. Similarly, the helicity angle $\cos\theta_\ell$ is partitioned into ten equally spaced bins covering the full physical range, $-1 \leq \cos\theta_\ell \leq 1$. Within each $(q^2, \cos\theta_\ell)$ bin, the corresponding M_X distribution is subdivided into the same coarse intervals used in the p_ℓ^B analysis. A binned maximum-likelihood fit is then performed to extract the signal yield while statistically separating the $B \to X_c \ell \nu$ signal from $B\bar{B}$ and continuum background contributions. The post-fitted q_ℓ^2 in the fine bins of $1\ \mathrm{GeV}^2$ each for the electron and muon channels can be seen in A.1.1. Similarly, the post-fitting yields for $\cos\theta_\ell$ can be seen in A.1.2 for the electron and muon channels.

Therefore, fitting the M_X distribution in coarse bins within the p_ℓ^B, q^2 and $\cos\ \theta_\ell$ interval exploits the distinct kinematic and topological characteristics of signal and background processes, which populate different regions of the hadronic mass spectrum. This binning scheme preserves the essential shape information required for an effective statistical separation of the $B \to X_c \ell \nu$ signal from $B\bar{B}$ and continuum background contributions, while avoiding excessive statistical fluctuations arising from limited data and simulated sample sizes.

6.3 Efficiency Corrections

The signal reconstruction efficiency is evaluated as a function of the lepton momentum in the B meson rest frame p_ℓ^B, the momentum transfer squared q^2, and the lepton helicity angle $\cos\theta_\ell$, in order to account for variations in detector acceptance, reconstruction performance, and event selection efficiency across different regions of the phase space. Consequently, an explicit determination of the signal efficiency in each kinematic bin is required to ensure an unbiased extraction of the differential observables.

For each bin i in p_ℓ^B, q^2, and $\cos\theta_\ell$, the signal efficiency is defined as

$$\varepsilon_i = \frac{N_{\mathrm{reco},i}}{N_{\mathrm{gen},i}}, \tag{6.2}$$

where $N_{\mathrm{reco},i}$ denotes the number of signal events that are successfully reconstructed and pass all analysis selection criteria in the i-th kinematic bin, and $N_{\mathrm{gen},i}$ corresponds to the number of generated signal events in the same bin at the generator level, prior to detector simulation and event reconstruction.

The efficiencies are determined using simulated signal samples and are evaluated independently in each bin to accurately capture the kinematic dependencies associated with tracking efficiency, particle identification performance, and selection requirements. In this work, we determine the efficiency in dependence of the lepton momentum p_ℓ^B, as well as on q^2 and $\cos\theta_\ell$, reflecting the interplay between detector acceptance and the underlying decay kinematics.

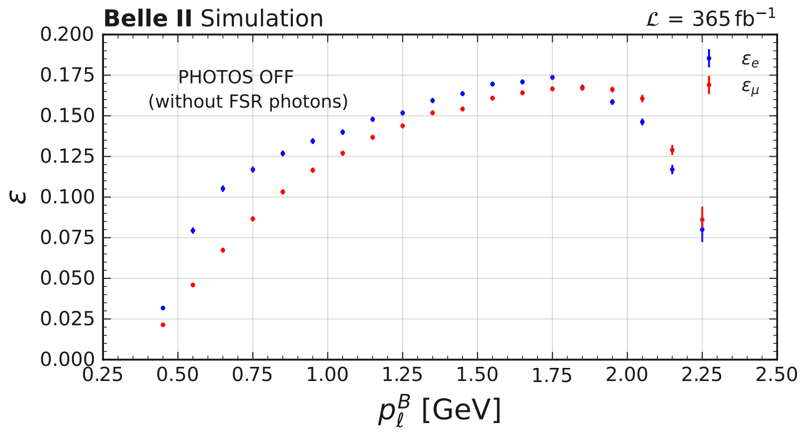

(a) ϵ_e and ϵ_μ in bins of the lepton momentum p_ℓ^B.

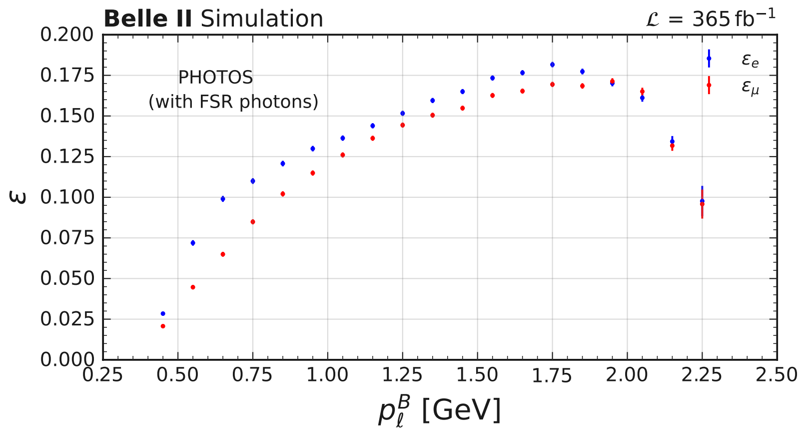

(b) ϵ_e and ϵ_μ in bins of the lepton momentum p_ℓ^B.

Figure 6.9: ε in bins of the lepton momentum p_ℓ^B, with and without the effect of the final state radiation photons.

The resulting efficiency distributions as a function of p_ℓ^B for the electron and muon channels are shown in Fig. 6.9(a). Variations in the efficiency across the lepton momentum spectrum are observed, especially at low and high momenta, where reconstruction and identification efficiencies differ for electrons and muons. The efficiency corrections are also calculated for samples that include the final-state radiation photons using the PHOTOS[14] simulation and can be seen in Fig. 6.9(b). The comparison of bin by bin efficiency correction for each lepton channel with and without the effect of FSR photons can be visualized in A.9(a) and A.9(b).

The extracted efficiencies are applied as bin-by-bin correction factors to the fitted signal yields in each kinematic interval. The combined application of efficiency and migration matrix corrections enables the determination of the fully unfolded spectra of the kinematic variables, p_ℓ^B, q^2, and $\cos\theta_\ell$.

6.4 Unfolding

The unfolded distributions of the kinematic observables are obtained by correcting the post-fit signal yields for detector effects, reconstruction inefficiencies, and bin-to-bin migration. The unfolding procedure combines the results of the signal yield extraction, the efficiency corrections, and the migration matrix in order to recover the underlying true distributions at the generator or truth level.

This is performed according to

$$\text{Unfolded Spectrum} = \mathbf{M}^{-1}\,\varepsilon^{-1} \cdot N^{X_c\ell\nu}_{\text{post-fit}} \tag{6.3}$$

where $N^{X_c\ell\nu}_{\text{post-fit}}$ denotes the signal yields obtained from the binned maximum-likelihood fits to the M_X distributions in each kinematic variable bin. These fitted yields represent the reconstructed-level signal distributions and therefore require correction for detector effects before physical interpretations can be made.

The ε contains the bin-by-bin signal reconstruction efficiencies evaluated as a function of the relevant kinematic variables, as described in Sec. 6.3. The inverse efficiency correction accounts for variations in detector acceptance, reconstruction performance, and event selection efficiency across the phase space. The migration matrix $\mathbf{M}$ is derived from simulated signal samples and accounts for bin-to-bin smearing in the measured observables as explained in Sec. 6.1. Applying these corrections corrects the smearing effects and ensures that the unfolded distributions are normalized to the number of generated signal events in each bin, restoring the true kinematic information.

The unfolding procedure is carried out independently for samples reconstructed with and without FSR photons. This separation allows for a consistent treatment of radiative effects. Both cases are treated consistently. The comparison of the unfolded distributions calculated using Eq. 6.3 and the true-level spectrum for p^B_ℓ, q^2_ℓ and cos θ_ℓ can be seen in Fig. 6.10, Fig. 6.11 and Fig. 6.12 respectively.

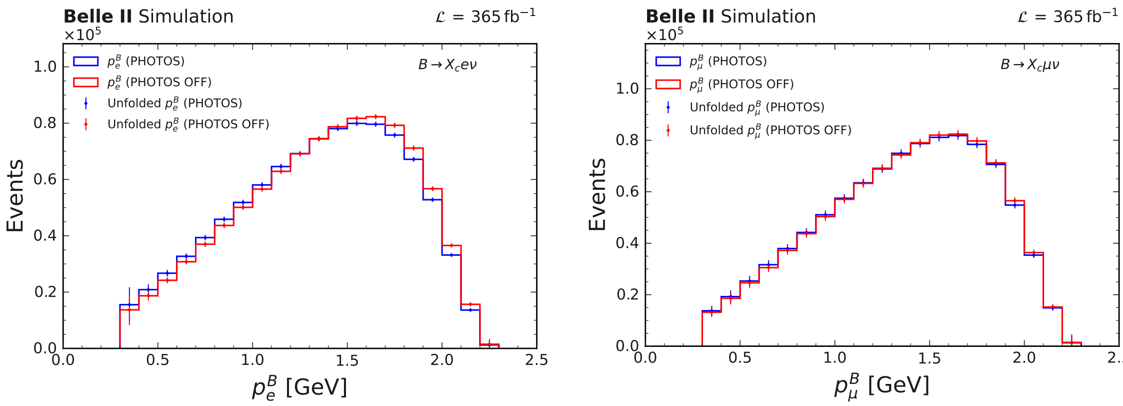

Figure 6.10: Unfolded distributions of p^B_ℓ with (blue) and without (red) FSR photons. It is compared to the truth-level p^B_ℓ spectrum as a cross-check to validate the unfolding procedure.

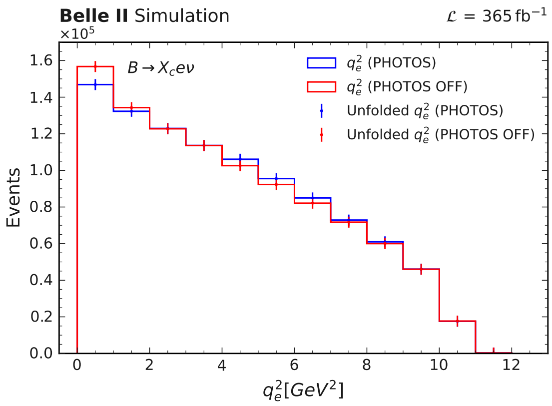

Figure 6.11: Unfolded distributions q_ℓ^2 with (blue) and without (red) FSR photons. It is compared to the truth-level q_ℓ^2 spectrum as a cross-check to validate the unfolding procedure.

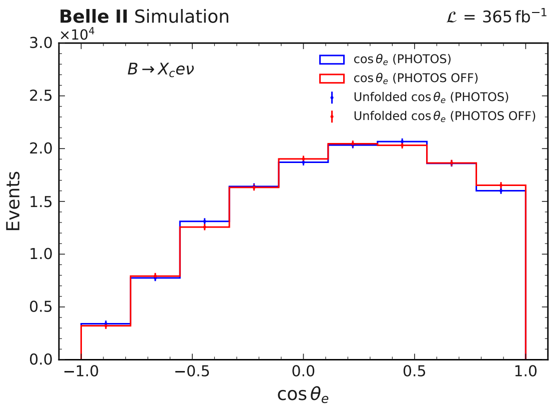

Figure 6.12: Unfolded Distributions of cos θ_ℓ with (blue) and without (red) FSR photons. It is compared to the truth-level cos θ_ℓ spectrum as a cross-check to validate the unfolding procedure.

The comparison of the unfolded spectra with and without the inclusion of FSR demonstrates that the largest impact is seen in the lepton momentum distribution p_ℓ^B, where FSR slightly shifts events toward lower momenta due to energy carried away by radiated photons. For the momentum transfer squared q^2, the effect is modest and primarily visible at low q^2. In contrast, the angular observable cos θ_ℓ shows only minimal sensitivity to FSR effects, since it depends primarily on the direction rather than the magnitude of the lepton momentum. Overall, the unfolded distributions obtained with and without FSR corrections remain consistent within uncertainties, indicating that the unfolding procedure is stable. By correcting the measured signal yields for detector and reconstruction effects, the unfolding enables a direct comparison of the experimental results with theoretical predictions at the generator level.

6.5 Branching Ratio and test of LFU

In this section, the inclusive branching ratio of the decay $B \to X_c \ell \nu_\ell$ is determined. The analysis is split into the electron and muon channels, but it combines charged and neutral B mesons, i.e., B^+ and B^0 produced in $\Upsilon(4S)$ decays.

The $\Upsilon(4S)$ resonance decays exclusively into B^+B^- and $B^0\bar{B}^0$ pairs. Since the two species have slightly different lifetimes, their contributions have to be properly accounted for. The average lifetime of the B meson is defined as

$$\tau_{\text{avg}} = \frac{\tau(B^+) + \tau(B^0)}{2} = (1.575 \pm 0.004)\ \text{ps}. \tag{6.4}$$

The production fractions of charged and neutral B mesons in $\Upsilon(4S)$ decays are denoted by

$$f_{+-} \quad \text{and} \quad f_{00},$$

respectively, with the constraint $f_{+-} + f_{00} = 1$ The values of the production fractions are obtained from the *HFLAV* average [23] which is used in later calculations.

The absolute branching fraction is determined from the measured signal yields obtained through template fitting, after applying the efficiency corrections described in Sec. 6.2 and Sec. 6.3. The branching ratio is calculated as

$$\mathcal{B}(B \to X_c \ell \nu_\ell) = \frac{N^{\ell}_{\text{sig}}\, \tau}{2N_{B\bar{B}}\, \varepsilon^{\ell}\, (f_{+-}\, \tau(B^+) + f_{00}\, \tau(B^0))}, \tag{6.5}$$

where N^{ℓ}_{sig} is the number of signal events extracted from the template fitting of each fine kinematic p^B_ℓ bin (0.1 GeV) in the three coarse bins of the charm hadronic mass M_X. The signal yields for the B^+ and B^0 are obtained separately, but the sum of the two is used in the ratio calculation. $N_{B\bar{B}}$ is the total number of produced $B\bar{B}$ pairs in the data sample. For each lepton momentum bin of 0.1 GeV (as explained in Sec. 6.2) in the B meson rest frame, the signal yields are corrected for reconstruction and selection efficiencies in that bin. Thus, first the differential branching fractions are computed separately for the electron and muon channels as functions of the lepton momentum thresholds using Eq. 6.5. The efficiency correction is given by ε^{ℓ} and is obtained from Eq. 6.2.f_{+-} and f_{00} are the corresponding production fractions, $\tau(B^+)$ and $\tau(B^0)$ are the lifetimes. The factor of 2 in the denominator accounts for the fact that each $\Upsilon(4S)$ decay produces two B mesons, both of which can contribute to the signal events. The absolute branching ratio in the lepton momentum thresholds is obtained by summing over all bins. The statistical uncertainties on the branching ratio arise from the uncertainties on the fitted signal yields.

The inclusive branching ratio measured in the electron and muon channels for a lepton momentum threshold $p^B_\ell > 0.3$ GeV without extrapolation to $p^B_\ell = 0$ GeV is calculated to be:

$$\mathcal{B}(B \to X_c e \nu_e; p^B_e > 0.3\,\text{GeV}) = (10.141 \pm 0.055\ (\text{stat}))\% \tag{6.6}$$

$$\mathcal{B}(B \to X_c \mu \nu_\mu; p^B_\mu > 0.3\,\text{GeV}) = (10.105 \pm 0.052\ (\text{stat}))\% \tag{6.7}$$

A direct test of lepton flavor universality (LFU) is performed by taking the ratio of the electron and muon branching fractions:

$$R(e/\mu) \equiv \frac{\mathcal{B}(B \to X_c e \nu_e)}{\mathcal{B}(B \to X_c \mu \nu_\mu)} = 1.004 \pm 0.008\ (\text{stat}). \tag{6.8}$$

The ratio is consistent with unity within the quoted statistical uncertainty, indicating no evidence for lepton flavor universality violation in inclusive semileptonic B decays within the current experimental precision.

The measured branching ratios are consistent with the expectations assumed in the analysis, indicating that the procedure reliably reproduces the input values. Consequently, the extracted signal yields correspond to the expectation values of the fitted model parameters. The use of Asimov data allows validation of the fitting framework and assessment of the expected statistical precision. The small statistical uncertainties demonstrate the internal consistency of the signal extraction procedure and the stability of the efficiency corrections. Therefore, the agreement between the electron and muon channels primarily demonstrates the consistency of the analysis framework and the absence of intrinsic biases in the fitting and efficiency correction procedures. The ratio $R(e/\mu)$ provides an important internal cross-check of the SM prediction of lepton flavor universality in charged-current interactions. Within the Asimov framework, the result is expected to be consistent with unity by construction. This observed agreement therefore validates the numerical implementation of the branching fraction extraction.

CHAPTER 7

Systematics

In addition to statistical uncertainties arising from the finite size of the data sample, measurements at Belle II are subject to systematic uncertainties originating from imperfect knowledge of the detector performance, reconstruction algorithms, and modeling of physical processes in MC simulations. Systematic uncertainties not only affect the normalization but also the shape of the kinematic distributions. Therefore, a careful evaluation and propagation of systematic uncertainties is essential for precision measurements.

Several sources contribute to the systematic uncertainty in this analysis. Detector-related uncertainties arise from differences between data and simulation in the reconstruction efficiency of charged particles and particle identification (PID). Another important source of systematic uncertainty originates from the reconstruction of the tag-side B meson using the FEI algorithm. Differences in tagging efficiency between data and MC simulation are corrected using calibration factors derived from control samples, and the residual mismodeling is propagated as a systematic uncertainty. Modeling of signal and background processes in the MC simulation constitutes an additional source of systematic uncertainty. In semileptonic B decays, uncertainties in the branching fractions of exclusive modes can affect the predicted shapes and normalizations of the templates used in the fit. Furthermore, uncertainties in the form-factor parameterizations used to describe these decays can alter the kinematic distributions of the final-state particles.

The propagation of systematic uncertainties is performed using the `SysVar`[11] framework, which generates variations of the relevant calibration constants and correction factors. The associated systematic effects are then implemented as *nuisance parameters* in the likelihood model. These parameters represent quantities that are not of direct physical interest but influence the measurement through detector effects, reconstruction efficiencies, or modeling uncertainties. In template-based likelihood fits, nuisance parameters modify either the normalization or the shape of the predicted distributions and are constrained by prior information reflecting the estimated uncertainty. During the likelihood maximization, these parameters are profiled, allowing the fit to account for systematic variations while extracting the parameters of interest. This procedure ensures that both statistical and systematic uncertainties are consistently propagated to the final measurement.

In this analysis, all systematic uncertainties are evaluated in bins of the lepton momentum in the B rest frame p_ℓ^B, using the threshold values used for the partial branching fraction measurement. For each threshold, the full analysis chain is repeated using systematically varied correction factors, and the resulting variations in the measured observable are used to determine the systematic uncertainty.

7.1 Branching Fraction Variations

Uncertainties in the branching fractions of exclusive semileptonic B decays such as $B \to D\ell\nu$ and $B \to D^*\ell\nu$, as well as the modeling of higher excited charm states (D^{**}) and non-resonant contributions, constitute an important source of systematic uncertainty in this analysis. The D^{**} states denote excited charm resonances, including D_1, D_1', D_2^*, and D_0^*, which contribute to the inclusive $B \to X_c\ell\nu$ decay spectrum. These uncertainties affect both the normalization and the kinematic distributions of the simulated signal component. To propagate these effects consistently through the analysis, up and down variations within the uncertainties of the known branching fractions are implemented using the `SysVar` framework. The framework generates correlated variations of MC templates based on the relevant semileptonic decay modes contributing to the inclusive $B \to X_c\ell\nu$ spectrum. For each decay mode, the branching fraction is varied within its uncertainty and the resulting event weights are recalculated. These variations modify the relative contributions of the different semileptonic decay channels and therefore change the shape of only the $B \to X_c\ell\nu$ signal templates. The resulting variations are implemented as systematic shape uncertainties in the statistical model.

7.2 Form Factor Modelling

Semileptonic B decays are described by form factors (FF), which encode the low-energy dynamics of the $B \to X_c\ell\nu$ decay. The modeling of these decays depends on the chosen FF parameterization. The `HAMMER` framework [24] is used to compute the FF reweighting factors in this analysis. In this work, the following parameterizations are employed:

- $B \to D\ell\nu$ and $B \to D^*\ell\nu$ decays are modeled using the BLPRXP parameterization [25].
- $B \to D^{**}\ell\nu$ decays are described using the BLR model [26], which provides separate parameter sets for the narrow and broad excited charm states.

The `SysVar` framework propagates these uncertainties while accounting for their correlations by directly using the corresponding up and down variations of the BLPRXP and BLR form factor parameterizations to produce modified signal templates. These variations are implemented as systematic shape uncertainties in the fit.

7.3 Tracking Efficiency

The tracking efficiency uncertainty arises from imperfect knowledge of the efficiency with which charged particle trajectories are reconstructed in the Belle II tracking detectors, primarily the Central Drift Chamber (CDC) and the Vertex Detector (VXD). Differences between data and simulation can occur due to detector alignment effects, imperfect modeling of detector material, hit reconstruction inefficiencies, and variations in track finding performance in environments with different track multiplicities. In semileptonic B decays, these effects mainly influence the reconstruction of charged particles belonging to the hadronic system X_c. Since the probability of missing tracks increases with the number of reconstructed particles in the event, the uncertainty is parameterized as a function of the ROE track multiplicity.

The uncertainty is propagated using the `Sysvar` framework. The tracking efficiency correction is parameterized as a function of the number of reconstructed tracks in the ROE. The systematic uncertainty increases with the number of tracks, reflecting the larger probability of reconstruction inefficiencies in higher track multiplicities, and is treated as fully correlated across all bins, corresponding to a global uncertainty in the tracking efficiency calibration. The reweighting procedure is performed by `Sysvar`, which generates up/down variations of the tracking efficiency corrections and propagates them through the analysis ensuring a consistent treatment of correlations when the variations are incorporated as nuisance parameters in the statistical fit. The covariance and correlation matrices for the varied correction factors, properly accounting for correlations based on the sign of the variations, are presented in Fig 7.1.

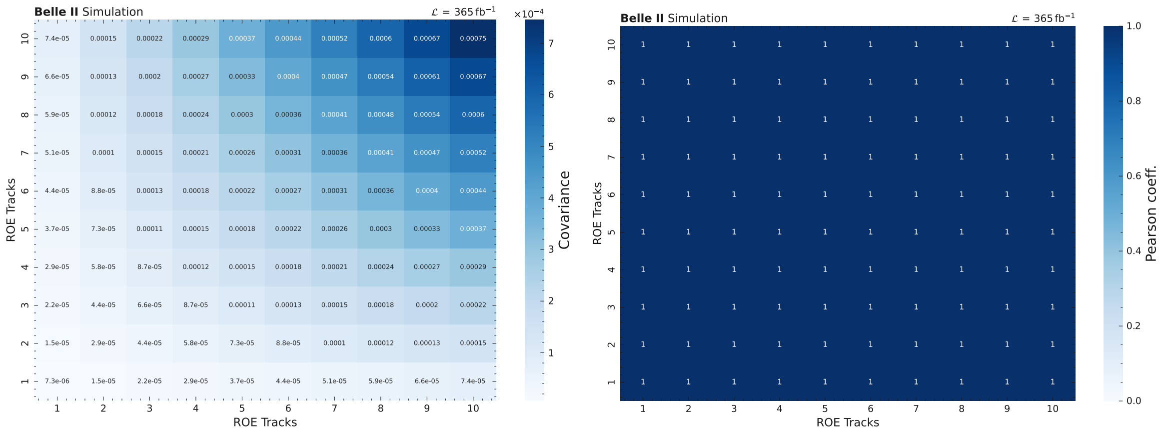

Figure 7.1: Covariance (left) and correlation (right) matrices for the uncertainty in the tracking efficiency obtained from `SysVar` after incorporating the correction factors.

7.4 FEI Tagging Efficiency

The reconstruction of the tag-side B meson is performed using the FEI algorithm. Since the FEI reconstruction efficiency differs between data and MC simulation, calibration factors derived from control samples are applied to correct for this difference. The associated uncertainties constitute a systematic uncertainty on the tag-side reconstruction. These corrections depend on the reconstructed tag mode and are implemented using calibration tables provided by the Belle II performance group.

`SysVar` performs internal reweighting of the MC events using the varied FEI correction tables based on the hadronic tagging mode. The shifts observed in each analysis bin under the up and down variations define the systematic deviations, which are used to construct the covariance and correlation matrices thereby accounting for bin-to-bin correlations based on the signs of the variations. This approach ensures a consistent propagation of the FEI systematic uncertainty and its correlations throughout the analysis. The FEI uncertainty primarily affects the $B \to X_c \ell \nu$ signal channel since the FEI algorithm is used to reconstruct the tag-side B meson for signal events. Variations in the FEI calibration therefore change the effective signal efficiency and propagate to the extracted signal yields as systematic shape uncertainties. The resulting covariance and correlation matrix, in Fig. 7.2 and Fig. 7.3, represents the propagated FEI systematic uncertainty for the B^+ tag and B^0 tag.

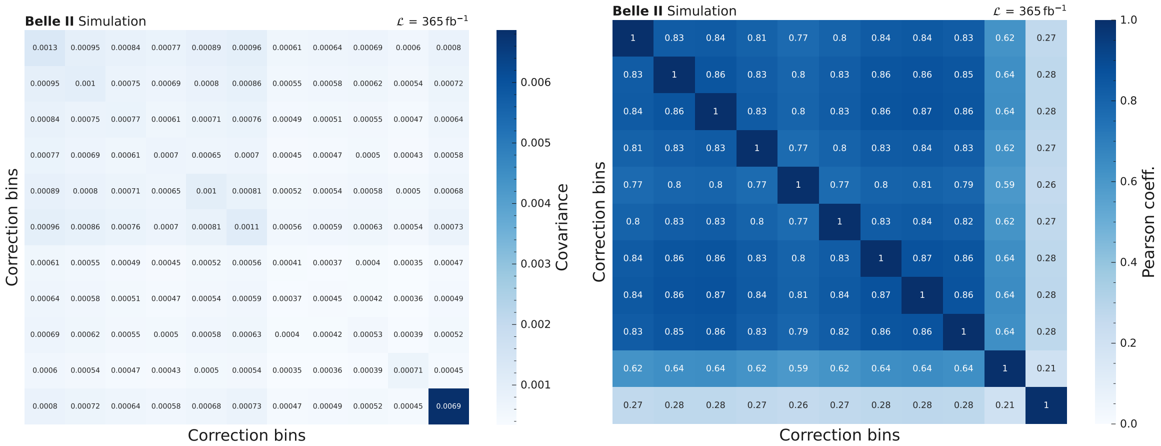

Figure 7.2: Covariance (left) and correlation (right) matrices for the FEI B^0 tag uncertainty obtained from `SysVar` after incorporating the correction factors.

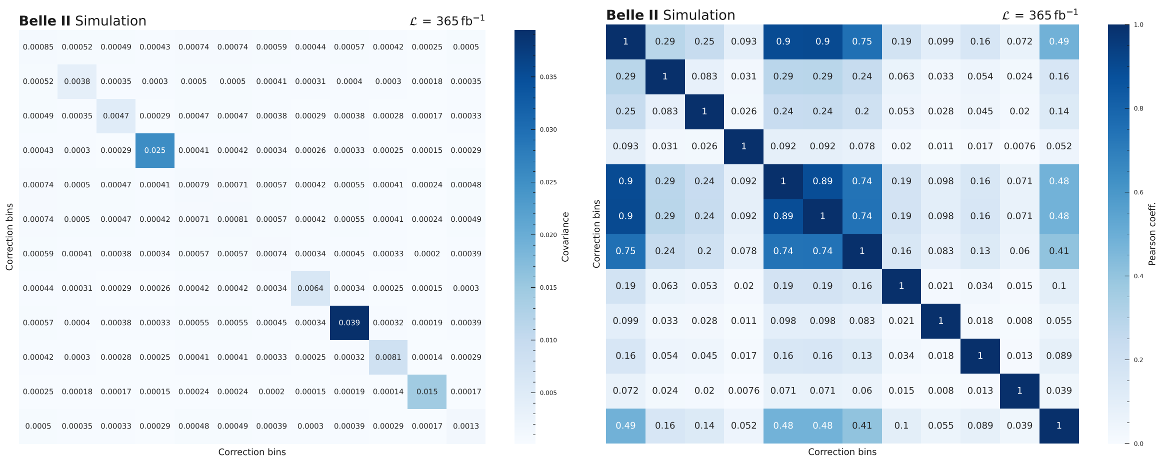

Figure 7.3: Covariance (left) and correlation (right) matrices for the FEI B^+ tag uncertainty obtained from `SysVar` after incorporating the correction factors.

7.5 Lepton Identification Corrections

The uncertainty on the lepton identification (lepton ID) efficiency is propagated using the `SysVar` tool, which automatically generates the corresponding variations for all relevant systematic sources, namely `lepID_eff`, `lepID_k_fake` and `lepID_pi_fake`. The component `lepID_eff` corresponds to the uncertainty in the efficiency with which true leptons (electrons or muons) are correctly identified by the particle identification (PID) algorithm. The `lepID_k_fake` and `lepID_pi_fake` components describe the uncertainties associated with the misidentification of kaons and pions, respectively, as leptons. These "fake" contributions arise from hadrons being incorrectly classified as leptons due to overlaps in detector response or limitations of the PID calibration.

The reweighting of events to account for these effects is performed by `SysVar`, using PID calibration tables to generate the varied correction factors corresponding to each systematic variation. These variations are propagated through the full analysis chain and are used to construct the covariance matrices of the systematic uncertainties on the measured observables.

Since particle identification affects the reconstruction and classification of leptons in all event categories, the PID uncertainty impacts not only the signal sample ($B \to X_c \ell \nu$) but also the $B\bar{B}$ background and continuum background ($e^+e^- \to q\bar{q}$) channels. The corresponding variations are therefore applied to all templates in the statistical model.

For this uncertainty, the electron and muon channels are treated as uncorrelated, since the PID performance and calibration procedures differ for the two lepton species. All other systematic uncertainties considered in this analysis are treated as correlated between the electron and muon channels.

Table 7.1 and Fig 7.4 summarize the nuisance parameters used in the statistical model. In this analysis, *categories* refer to the different event components entering the fit, namely the signal process $B \to X_c \ell \nu$, the generic $B\bar{B}$ background, and the continuum background from $e^+e^- \to q\bar{q}$. The term *modes* refers to the lepton flavor channels considered in the analysis, specifically the electron and muon channels. When systematic uncertainties are described as correlated between categories or modes, the corresponding nuisance parameter variations are applied simultaneously to the relevant components of the fit model via modifiers. *histosys* refers to the modifier in our `pyhf` fitting framework that introduces a correlated systematic for shape and normalization.

Table 7.1: Summary of nuisance parameters used in the fit, their implementation, type, and number of parameters.

Nuisance parameter	**Implementation**	**Type**	**# of NP**
$B \to X_c \ell \nu$ branching fractions	Individual NP for $B \to X_c \ell \nu$ with $X_c = [D, D^*, D_1, D_0^*, D_1', D_2^*, D^*\eta, D\eta, D\pi\pi, D^*\pi\pi]$. Correlated between lepton modes and the signal category.	histosys	10
Form factors	Variations along eigendirections: 8 BLPRXP variations for $D\ell\nu$ and $D^*\ell\nu$, and 6 + 4 BLR variations for $D^{**}\ell\nu$. Correlated between lepton modes and the signal category	histosys	18
FEI tagging efficiency	Split between B^+ and B^0; correlated between lepton modes and categories.	histosys	2
Tracking uncertainty	Correlated between all analysis categories and lepton modes.	histosys	1
Lepton ID	Toy-based variations combined into a single nuisance parameter direction each for lepton ID efficiency, lepton ID (fake K) and lepton ID (fake π). Uncorrelated across electron and muon modes.	histosys	3

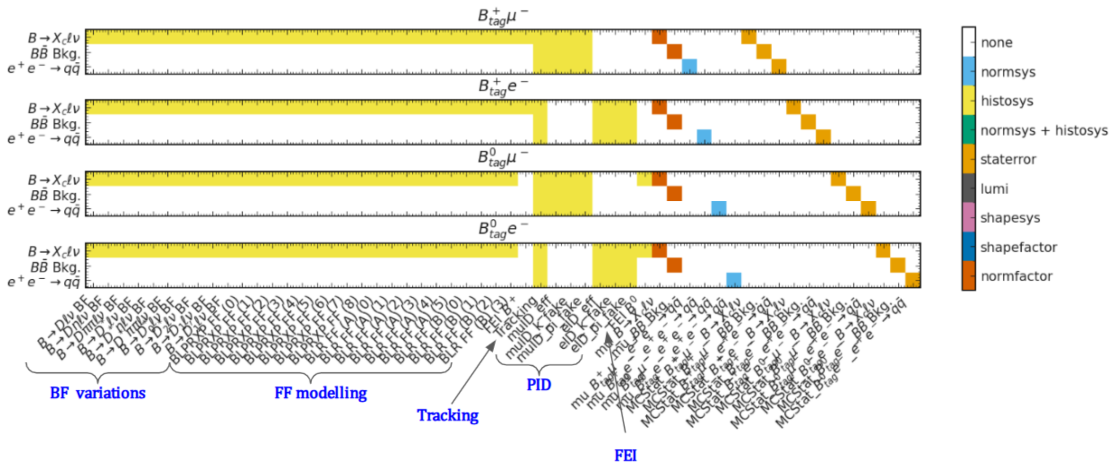

Figure 7.4: Complete systematic profile showing the three categories of $B \to X_c \ell \nu$ signal, $B\bar{B}$ background, and $e^+e^- \to q\bar{q}$ continuum background events in the electron and muon channels with the contribution of each systematic uncertainty.

The total systematic and statistical uncertainties in the p_ℓ^B thresholds for the electron and muon channels are presented in Table 7.2 and Table 7.3.

Table 7.2: Systematic uncertainties in p_e^B thresholds (uncertainties in %).

p_e^B threshold	0.3	0.4	0.5	0.6	0.7	0.8	0.9	1	1.1	1.2	1.3	1.4	1.5	1.6	1.7	1.8	1.9	2.0	2.1	2.2
$\mathcal{B}(B \to De\nu)$	0.42	0.42	0.43	0.43	0.43	0.41	0.41	0.39	0.37	0.33	0.32	0.27	0.24	0.20	0.17	0.13	0.07	0.05	0.02	0.01
$\mathcal{B}(B \to D^*e\nu)$	0.96	0.96	0.97	0.96	0.97	0.91	0.85	0.79	0.74	0.66	0.62	0.54	0.50	0.43	0.34	0.19	0.09	0.07	0.05	0.03
$\mathcal{B}(B \to D_1e\nu)$	0.65	0.64	0.61	0.58	0.54	0.50	0.44	0.42	0.39	0.30	0.24	0.17	0.09	0.06	0.04	0.03	0.01	0.00	0.00	0.00
$\mathcal{B}(B \to D_0^*e\nu)$	0.58	0.57	0.55	0.54	0.49	0.44	0.43	0.40	0.33	0.24	0.19	0.13	0.09	0.06	0.04	0.02	0.01	0.01	0.00	0.00
$\mathcal{B}(B \to D_1'e\nu)$	0.48	0.45	0.44	0.42	0.48	0.39	0.38	0.34	0.28	0.20	0.17	0.12	0.08	0.06	0.05	0.03	0.02	0.02	0.01	0.00
$\mathcal{B}(B \to D_2^*e\nu)$	0.32	0.31	0.34	0.29	0.34	0.27	0.20	0.13	0.09	0.07	0.05	0.03	0.03	0.02	0.02	0.01	0.01	0.01	0.00	0.00
$\mathcal{B}(B \to D^{**}e\nu)$	1.04	1.01	0.99	0.95	0.94	0.82	0.75	0.68	0.59	0.44	0.35	0.24	0.16	0.11	0.08	0.05	0.03	0.02	0.01	0.00
$\mathcal{B}(B \to D\eta e\nu)$	0.21	0.22	0.22	0.21	0.18	0.14	0.12	0.09	0.08	0.07	0.05	0.05	0.04	0.03	0.02	0.02	0.01	0.01	0.00	0.00
$\mathcal{B}(B \to D^*\eta e\nu)$	0.24	0.23	0.22	0.20	0.18	0.15	0.12	0.10	0.09	0.08	0.07	0.05	0.03	0.03	0.02	0.02	0.01	0.01	0.00	0.00
$\mathcal{B}(B \to D\pi\pi e\nu)$	0.18	0.17	0.18	0.17	0.14	0.15	0.12	0.09	0.07	0.04	0.04	0.03	0.02	0.01	0.01	0.01	0.01	0.01	0.01	0.00
$\mathcal{B}(B \to D^*\pi\pi e\nu)$	0.21	0.20	0.19	0.17	0.13	0.10	0.09	0.08	0.08	0.07	0.06	0.05	0.04	0.03	0.03	0.02	0.01	0.01	0.01	0.01
$\mathcal{B}(B \to \text{Gap Modes})$	0.42	0.41	0.41	0.37	0.31	0.27	0.22	0.19	.17	0.14	0.12	0.10	0.07	0.06	0.04	0.04	0.02	0.02	0.01	0.01
FF (BLPRXP)	0.05	0.05	0.06	0.05	0.05	0.05	0.04	0.04	0.04	0.03	0.03	0.03	0.02	0.02	0.03	0.02	0.02	0.01	0.01	0.01
FF BLR 1	0.51	0.57	0.56	0.54	0.55	0.58	0.51	0.51	0.49	0.46	0.34	0.38	0.27	0.23	0.18	0.15	0.11	0.10	0.09	0.05
FF BLR 2	0.04	0.04	0.04	0.04	0.04	0.04	0.04	0.04	0.04	0.03	0.04	0.03	0.03	0.02	0.02	0.02	0.01	0.00	0.01	0.01
Efficiency Corrections	0.13	0.15	0.21	0.22	0.21	0.21	0.20	0.19	0.19	0.18	0.18	0.18	0.18	0.18	0.18	0.19	0.20	0.22	0.22	0.19
Tracking	0.26	0.25	0.25	0.25	0.26	0.26	0.24	0.25	0.25	0.26	0.25	0.24	0.24	0.24	0.25	0.24	0.25	0.24	0.24	0.24
Electron ID	0.17	0.17	0.17	0.17	0.16	0.17	0.18	0.17	0.16	0.12	0.15	0.17	0.17	0.16	0.15	0.15	0.15	0.14	0.14	0.12
Electron ID (fake π)	0.06	0.06	0.06	0.06	0.06	0.06	0.05	0.05	0.05	0.05	0.04	0.04	0.04	0.03	0.01	0.02	0.02	0.01	0.00	0.00
Electron ID (fake K)	0.03	0.03	0.03	0.03	0.03	0.02	0.02	0.03	0.01	0.02	0.02	0.02	0.02	0.02	0.01	0.01	0.01	0.01	0.00	0.00
FEI B^0	0.07	0.07	0.08	0.07	0.08	0.08	0.08	0.08	0.08	0.09	0.09	0.09	0.09	0.09	0.09	0.08	0.08	0.08	0.08	0.08
FEI B^+	0.14	0.16	0.16	0.15	0.17	0.16	0.15	0.16	0.16	0.17	0.17	0.18	0.17	0.17	0.16	0.15	0.15	0.06	0.04	0.03
Statistical	0.055	0.055	0.055	0.055	0.056	0.056	0.056	0.054	0.056	0.056	0.056	0.054	0.054	0.054	0.055	0.055	0.054	0.054	0.054	0.054
Systematic	1.6654	1.6639	1.6632	1.6142	1.6043	1.5015	1.3894	1.3048	1.2126	1.0634	0.9452	0.8601	0.7591	0.6690	0.5793	0.4720	0.4290	0.3970	0.3848	0.3483
Total	1.6663	1.6648	1.6641	1.6152	1.6052	1.5025	1.3905	1.3059	1.2138	1.0648	0.9468	0.8616	0.7610	0.6710	0.5816	0.4748	0.4323	0.4004	0.3881	0.3519

Table 7.3: Systematic uncertainties in p_μ^B thresholds (uncertainties in %).

p_μ^B threshold	0.3	0.4	0.5	0.6	0.7	0.8	0.9	1	1.1	1.2	1.3	1.4	1.5	1.6	1.7	1.8	1.90	2.0	2.1	2.2
$\mathcal{B}(B \to D\mu\nu)$	0.40	0.40	0.41	0.41	0.41	0.39	0.39	0.37	0.35	0.31	0.29	0.26	0.23	0.19	0.16	0.12	0.07	0.05	0.02	0.01
$\mathcal{B}(B \to D^*\mu\nu)$	0.91	0.91	0.91	0.92	0.92	0.87	0.81	0.75	0.71	0.63	0.59	0.55	0.48	0.41	0.32	0.18	0.09	0.07	0.05	0.03
$\mathcal{B}(B \to D_1\mu\nu)$	0.64	0.63	0.64	0.63	0.61	0.57	0.51	0.43	0.37	0.29	0.23	0.16	0.09	0.06	0.04	0.03	0.01	0.00	0.00	0.00
$\mathcal{B}(B \to D_0^*\mu\nu)$	0.55	0.54	0.52	0.51	0.50	0.49	0.45	0.38	0.31	0.23	0.18	0.12	0.09	0.06	0.04	0.02	0.01	0.01	0.00	0.00
$\mathcal{B}(B \to D_1'\mu\nu)$	0.45	0.44	0.45	0.44	0.43	0.41	0.36	0.32	0.27	0.19	0.16	0.10	0.08	0.06	0.05	0.03	0.02	0.01	0.00	0.00
$\mathcal{B}(B \to D_2^*\mu\nu)$	0.33	0.33	0.34	0.33	0.32	0.26	0.19	0.12	0.09	0.07	0.05	0.03	0.03	0.02	0.02	0.01	0.01	0.00	0.00	0.00
$\mathcal{B}(B \to D^{(**)}\mu\nu)$	1.01	1.00	1.00	0.98	0.95	0.89	0.79	0.67	0.56	0.42	0.34	0.23	0.15	0.10	0.08	0.05	0.03	0.01	0.00	0.00
$\mathcal{B}(B \to D\eta\mu\nu)$	0.22	0.21	0.21	0.20	0.17	0.13	0.11	0.09	0.08	0.07	0.05	0.05	0.04	0.03	0.02	0.02	0.01	0.01	0.00	0.00
$B \to D^*\eta\mu\nu$	0.24	0.22	0.21	0.19	0.17	0.14	0.11	0.10	0.09	0.08	0.07	0.05	0.03	0.03	0.02	0.02	0.01	0.01	0.00	0.00
$\mathcal{B}(B \to D\pi\pi\mu\nu)$	0.17	0.16	0.17	0.16	0.13	0.14	0.11	0.09	0.07	0.04	0.04	0.03	0.02	0.01	0.01	0.01	0.01	0.01	0.01	0.00
$\mathcal{B}(B \to D^*\pi\pi\mu\nu)$	0.19	0.19	0.18	0.16	0.12	0.10	0.09	0.08	0.08	0.07	0.06	0.05	0.04	0.03	0.03	0.02	0.01	0.01	0.01	0.01
$\mathcal{B}(B \to$ Gap Modes$)$	0.41	0.39	0.39	0.36	0.30	0.26	0.21	0.18	0.16	0.13	0.11	0.09	0.07	0.05	0.04	0.03	0.02	0.02	0.01	0.01
FF (BLPRXP)	0.05	0.05	0.06	0.05	0.05	0.05	0.04	0.04	0.04	0.03	0.03	0.03	0.02	0.02	0.03	0.02	0.02	0.01	0.01	0.01
FF BLR 1	0.51	0.54	0.53	0.51	0.52	0.55	0.49	0.48	0.47	0.44	0.32	0.36	0.26	0.22	0.17	0.14	0.09	0.05	0.02	0.01
FF BLR 2	0.04	0.04	0.04	0.04	0.04	0.04	0.04	0.04	0.04	0.03	0.04	0.03	0.03	0.02	0.02	0.02	0.01	0.00	0.01	0.01
Efficiency Corrections	0.03	0.12	0.16	0.17	0.18	0.18	0.18	0.17	0.17	0.17	0.17	0.17	0.17	0.17	0.17	0.18	0.21	0.24	0.25	0.17
Tracking	0.26	0.25	0.25	0.25	0.26	0.26	0.24	0.25	0.25	0.26	0.25	0.24	0.24	0.24	0.25	0.24	0.25	0.24	0.24	0.24
Muon ID	0.19	0.19	0.19	0.19	0.19	0.17	0.18	0.17	0.16	0.14	0.15	0.17	0.17	0.16	0.15	0.15	0.15	0.14	0.14	0.12
Muon ID (fake π)	0.06	0.06	0.06	0.06	0.06	0.06	0.05	0.05	0.05	0.05	0.04	0.04	0.04	0.03	0.01	0.02	0.02	0.01	0.00	0.00
Muon ID (fake K)	0.03	0.03	0.03	0.03	0.03	0.02	0.02	0.03	0.01	0.02	0.02	0.02	0.02	0.02	0.01	0.01	0.01	0.01	0.00	0.00
FEI B^0	0.07	0.07	0.08	0.07	0.08	0.08	0.08	0.08	0.08	0.09	0.09	0.09	0.09	0.09	0.09	0.08	0.08	0.08	0.08	0.08
FEI B^+	0.13	0.15	0.15	0.14	0.16	0.15	0.14	0.15	0.15	0.16	0.16	0.17	0.16	0.16	0.15	0.14	0.14	0.06	0.04	0.03
Statistical	0.052	0.052	0.052	0.053	0.053	0.052	0.053	0.053	0.053	0.052	0.053	0.053	0.053	0.052	0.053	0.053	0.053	0.052	0.052	0.052
Systematic	1.6045	1.5998	1.6007	1.5792	1.5583	1.4873	1.3588	1.2405	1.1431	1.0031	0.8877	0.8275	0.7062	0.6191	0.5303	0.4217	0.3631	0.3117	0.2974	0.2834
Total	1.6053	1.6007	1.6016	1.5801	1.5592	1.4883	1.3598	1.2416	1.1443	1.0045	0.8892	0.8291	0.7080	0.6212	0.5327	0.4246	0.3666	0.3159	0.3017	0.2880

From Tables 7.2 and 7.3, it can be observed that the dominant systematic uncertainty across most lepton momentum thresholds arises from the uncertainties in the semileptonic branching fractions of the exclusive $B \to X_c\ell\nu$ decay modes. In particular, the contributions from the $B \to D^*\ell\nu$ and $B \to D\ell\nu$ channels constitute the largest fraction of the total systematic uncertainty, reflecting the strong dependence of the signal model on the assumed composition of the inclusive decay. Form factor modeling also contributes noticeably, especially through the BLPRXP variations for $B \to D^{(*)}\ell\nu$ and the BLR variations for $B \to D^{**}\ell\nu$ decays. Detector-related systematics such as tracking efficiency, particle identification, and FEI tagging efficiency are comparatively smaller and remain relatively stable across the lepton momentum thresholds. Overall, the systematic uncertainty decreases for higher p_ℓ^B thresholds due to the reduction of background contributions and the improved purity of the selected signal sample.

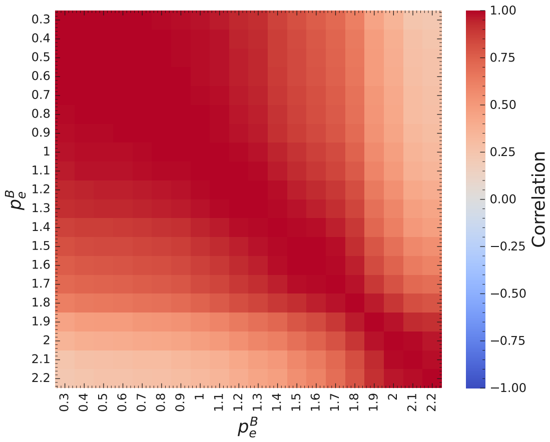

(a) Electron channel

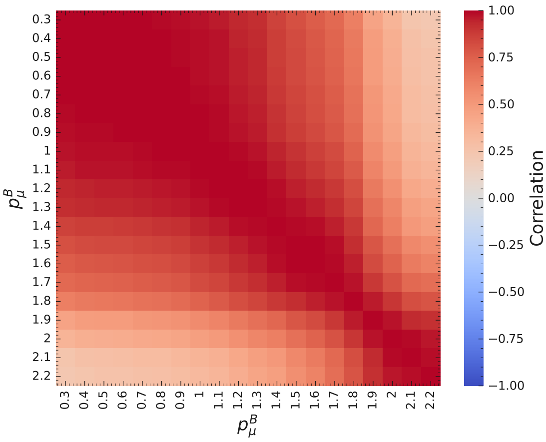

(b) Muon channel

Figure 7.5: Covariance matrices of the systematic uncertainties for the p_ℓ^B thresholds in the electron (left) and muon (right) channels.

Fig. 7.5 shows the correlation matrices of the systematic uncertainties across the different p_ℓ^B thresholds for the electron and muon channels. A strong positive correlation is observed between neighboring momentum thresholds. This arises mainly from the large overlap of the selected event samples at nearby thresholds, resulting in very similar systematic variations across these regions. The correlation gradually decreases for thresholds that are further apart in momentum, indicating that the systematic variations impact nearby kinematic regions more similarly than distant ones. The overall structure of the correlation matrices is consistent between the electron and muon channels, demonstrating that the dominant systematic effects are treated coherently across both lepton modes.

CHAPTER **8**

Extraction of Inclusive $|V_{cb}|$

8.1 The CKM Matrix

In the SM, quark flavor-changing weak interactions are described by the Cabibbo–Kobayashi–Maskawa (CKM) matrix. This unitary matrix relates the quark weak interaction eigenstates to their mass eigenstates and governs the strength of charged-current transitions between different quark flavors. The CKM matrix can be written as

$$V_{\mathrm{CKM}} = \begin{pmatrix} V_{ud} & V_{us} & V_{ub} \\ V_{cd} & V_{cs} & V_{cb} \\ V_{td} & V_{ts} & V_{tb} \end{pmatrix} \tag{8.1}$$

The matrix element $|V_{cb}|$ determines the strength of the transition between the b and c quarks and can be measured through semileptonic B meson decays of the form $B \to X_c \ell \nu$. Precise measurements of $|V_{cb}|$ are essential for testing the consistency of the SM and for constraining the unitarity of the CKM matrix.

8.2 Inclusive Determination of $|V_{cb}|$

Inclusive measurements of $|V_{cb}|$ are based on the total semileptonic decay rate for $B \to X_c \ell \nu$ processes, where X_c denotes any charmed hadronic final state. The theoretical description of these decays relies on the HQE, which expresses the inclusive decay rate as an expansion in powers of $\Lambda_{\mathrm{QCD}}/m_b$. Within the HQE framework, the inclusive decay rate can be written schematically as

$$\Gamma(B \to X_c \ell \nu) \propto |V_{cb}|^2 m_b^5 \left[1 + \frac{\alpha_s}{\pi} + \frac{\mu_\pi^2}{m_b^2} + \frac{\rho_D^3}{m_b^3} + \cdots \right], \tag{8.2}$$

where m_b is the b-quark mass and the parameters μ_π^2, μ_G^2, ρ_D^3, and ρ_{LS}^3 describe non-perturbative corrections associated with the motion and interactions of the heavy quark inside the B meson. The extraction of $|V_{cb}|$ therefore depends on a simultaneous determination of these HQE parameters from experimental observables.

8.3 Extraction Using the Kolya Framework

The determination of $|V_{cb}|$ in this analysis is performed using the Kolya framework[1], which implements a global fit of inclusive semileptonic observables within the HQE formalism. The framework incorporates perturbative QCD corrections and theoretical predictions for the relevant observables.

In this work, the measured partial branching fractions for the decay $B \to X_c \ell \nu$ at different thresholds of the lepton energy E_ℓ^B are used as input to the fit. In addition to the measured values, the full covariance matrix of statistical and systematic uncertainties obtained in this analysis is provided to the Kolya framework.

The fit procedure minimizes a χ^2 function that compares the experimental measurements with the theoretical predictions computed within the HQE framework,

$$\chi^2 = (\vec{M}_{\text{exp}} - \vec{M}_{\text{th}})^T C^{-1} (\vec{M}_{\text{exp}} - \vec{M}_{\text{th}}), \tag{8.3}$$

where $\vec{M}_{\text{exp}}$ represents the vector of measured observables, $\vec{M}_{\text{th}}$ denotes the theoretical predictions, and C is the covariance matrix containing the experimental uncertainties and correlations.

The fit simultaneously determines the value of $|V_{cb}|$ and the HQE parameters incorportaing the uncertainties that describe the inclusive decay dynamics. The parameters extracted in the fit include the heavy-quark masses m_b and m_c, the non-perturbative HQE parameters μ_π^2, μ_G^2, ρ_D^3, and ρ_{LS}^3, as well as the strong coupling constant α_s.

8.4 Fit Results

Using the measured partial branching fractions and their covariance matrix, the Kolya fit provides the central value of $|V_{cb}|$ together with the corresponding HQE parameters. The central values obtained in this analysis is listed in Table 8.1.

Table 8.1: Results of the sensitivities on $|V_{cb}|$ and the HQE parameters from the fit using the covariance matrix and uncertainties from this work.

	Central Value	Uncertainty
$\|V_{cb}\|$	42.351	0.246
$m_b^{\text{MS}}(m_b)$	4.174	0.004
$m_c^{\text{MS}}(3\,\text{GeV})$	1.004	0.005
$\alpha_s(m_Z)$	0.118	0.000
$\mu(m_b^{\text{kin}})$	1.203	0.020
$\mu(m_c^{\text{MS}})$	1.874	0.001
$\mu(\alpha_s)$	8.493	0.749
μ_π	0.387	0.008
μ_G	0.118	0.017
ρ_D	0.110	0.001
ρ_{LS}	0.067	0.058

Since the Kolya framework is designed for fits to measurements of inclusive $B \to X_c \ell \nu$ branching fractions and moments obtained from data, using results directly from simulated events is not sufficient. In simulation, the inclusive decay is modeled as a sum of exclusive channels, which does not fully represent the theoretical inclusive description used in the HQE framework.

To provide suitable inputs for the fit, an Asimov data set is constructed. In this approach, the central values of the observables are taken from theoretical expectations, while the uncertainties and correlations are derived from the sensitivities obtained in this analysis. The resulting Asimov data set is used as input to the `Kolya` fit together with the covariance matrix of the experimental uncertainties. The fit determines the value of $|V_{cb}|$ and the HQE parameters by minimizing a χ^2 function that compares the predicted HQE moments with the constructed Asimov data set.

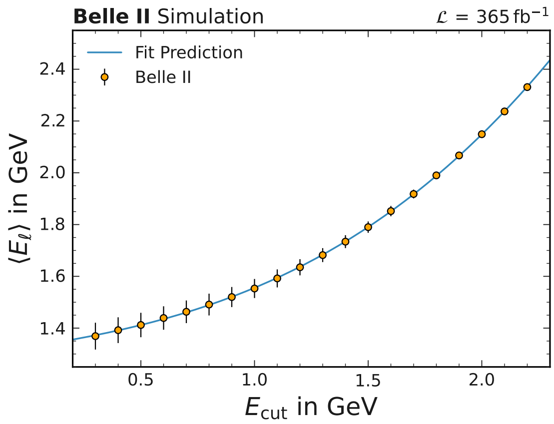

Figure 8.1: Orange data points, labeled as Belle II, display central values of the first E_ℓ moment. The uncertainties are according to the estimated sensitivities from this work. The blue line shows the best fit result for the HQE parameters and the respective predicted $\langle E_\ell \rangle$.

Fig. 8.1 shows the generated Asimov points for the first moment of the lepton energy as a function of the lepton energy threshold $E_{\mathrm{cut}} \in [0.3, 2.3]$ GeV, together with the result of the HQE fit. The orange data points represent the expected central values and uncertainties obtained from this analysis while the blue curve corresponds to the best-fit prediction from the HQE framework. The visible agreement between the fitted prediction and the generated data points demonstrates the sensitivity of the measured observable to the HQE parameters and the CKM matrix element $|V_{cb}|$.

CHAPTER 9

Results

This chapter presents the final results of the analysis. First, the measurement of the inclusive semileptonic branching fraction $B \to X_c \ell \nu$ is discussed. Subsequently, the extraction of the CKM matrix element $|V_{cb}|$ using the Heavy Quark Expansion (HQE) framework is presented.

The analysis first looks into the unfolding procedure of the kinematic variables of p_ℓ^B, q_ℓ^2 and $\cos\,\theta_\ell$ that incorporates detector efficiency and resolution/smearing effect corrections. It can be seen in Sec. 6.4 that the unfolding process established an exact match to the truth-level spectrum of the kinematic variables.

Further, the partial inclusive semileptonic branching fraction is measured in bins of the lepton momentum threshold. Signal yields are extracted using a template fit to the hadronic mass M_X distribution in each kinematic bin of the lepton momentum, and along with the efficiency corrections, it is used to determine the absolute $\mathcal{B}(B \to X_c \ell \nu)$.

Systematic uncertainties arising from detector effects, signal modeling, and calibration corrections are incorporated in the statistical model as nuisance parameters. These include uncertainties from branching fraction inputs, form factor modeling, FEI tagging efficiency, tracking efficiency, particle identification, and Monte Carlo statistical uncertainties. The correlations between these systematic sources are consistently treated within the statistical framework.

The inclusive branching ratios from the electron and muon channels, without extrapolation to $p_\ell^B = 0\,\text{GeV}$, are measured to be

$$\mathcal{B}(B \to X_c e \nu_e; p_e^B > 0.3\,\text{GeV}) = (10.141 \pm 0.055\ (\text{stat}))\%, \tag{9.1}$$

$$\mathcal{B}(B \to X_c \mu \nu_\mu; p_\mu^B > 0.3\,\text{GeV}) = (10.105 \pm 0.052\ (\text{stat}))\%. \tag{9.2}$$

The result is consistent between the electron and muon channels within uncertainties and agrees with previous measurements within the current experimental precision.

The CKM matrix element $|V_{cb}|$ is extracted using the `Kolya` framework, which performs a global χ^2 fit of HQE predictions to the measured observables. The fit uses the partial branching fractions in thresholds of the lepton energy E_ℓ^B obtained in this analysis together with their covariance matrix, which includes both statistical and systematic uncertainties.

The HQE framework describes inclusive semileptonic B decays as an expansion in powers of $1/m_b$, incorporating perturbative QCD corrections and non-perturbative parameters such as μ_π^2, μ_G^2, ρ_D^3, and ρ_{LS}^3. By fitting the predicted moments of the kinematic distributions to the measured values, the HQE parameters and $|V_{cb}|$ are determined simultaneously.

Since the fitting framework is designed for measurements derived from data, an Asimov data set is constructed using the expected central values of the energy moment. The uncertainties and correlations of the moments are taken from the sensitivities estimated in this work. The fit determines the distribution of the first lepton energy moment $\langle E_\ell \rangle$ with respect to the thresholds of the lepton energy $E_\ell^B \in [0.3, 2.3]$ GeV.

The resulting value of the CKM matrix element is

$$|V_{cb}| = (42.351 \pm 0.246) \times 10^{-3}. \tag{9.3}$$

The fit simultaneously determines the HQE parameters in the kinetic scheme, including the heavy quark masses and non-perturbative matrix elements. The extracted values are consistent with previous global fits within uncertainties.

The obtained value of $|V_{cb}|$ is consistent with previous inclusive determinations and demonstrates the sensitivity achievable with the measured observables. The uncertainties are dominated by the experimental precision of the partial branching fractions and the systematic uncertainties associated with the signal modeling.

The measurement contributes to improving the precision of inclusive $|V_{cb}|$ determinations and provides additional input to global HQE fits. With further analysis, the precision will improve significantly, enabling more precise determinations of $|V_{cb}|$ and more stringent tests of the SM.

CHAPTER 10

Summary and Outlook

This thesis presents a study of inclusive semileptonic B meson decays of the form $B \to X_c \ell \nu$ at the Belle II experiment. These decays provide a powerful probe of the weak interaction and play an essential role in determining the magnitude of the CKM matrix element $|V_{cb}|$. Precise measurements of $|V_{cb}|$ are crucial for testing the internal consistency of the SM and for constraining the unitarity of the CKM matrix.

The analysis reconstructs events using the hadronic tagging technique, where one B meson in the event is fully reconstructed using the FEI algorithm. This allows the four-momentum of the signal-side B meson to be inferred, enabling the reconstruction of key kinematic observables such as the lepton momentum p_ℓ^B, the momentum transfer squared q^2, and the lepton helicity angle $\cos\theta_\ell$. Signal candidates are selected in both the electron and muon channels, and the remaining particles in the event are combined to form the hadronic system X_c.

Signal yields are extracted by performing template fits to the hadronic mass M_X distributions in fine bins of the kinematic observables. The resulting spectra are corrected for detector resolution and acceptance effects using an unfolding procedure. The unfolding incorporates the smearing effects by constructing migration matrices and also corrects for the efficiency of the reconstruction. Systematic uncertainties arising from detector effects, signal modeling, and calibration corrections are evaluated using the `Sysvar` framework. These include uncertainties associated with semileptonic branching fractions, form factor modeling, FEI tagging efficiency, tracking efficiency, and particle identification. All systematic sources are implemented as nuisance parameters within the statistical model, allowing correlations between different channels and categories to be consistently treated.

Using the signal yields and the efficiency corrections, the inclusive semileptonic branching fraction $B \to X_c \ell \nu$ is determined as a function of the lepton momentum threshold. The measured partial branching fractions and their covariance matrices are subsequently used as inputs to extract the CKM matrix element $|V_{cb}|$ within the HQE framework. The extraction is performed using the `Kolya` fitting framework, which performs a χ^2 fit of the predicted HQE moments to the measured observables. The resulting value of the CKM matrix element is

$$|V_{cb}| = (42.35 \pm 0.25) \times 10^{-3}, \tag{10.1}$$

which is consistent with previous inclusive determinations within the current experimental precision.

The results presented in this thesis demonstrate the feasibility of performing precision measurements of inclusive semileptonic B decays at Belle II. As the experiment continues to accumulate significantly larger data samples, the statistical precision of the measurement will improve substantially. Future analyses will benefit from improved calibrations of detector performance, particularly in the areas of particle identification, tracking efficiency, and FEI tagging.

In addition, improved knowledge of exclusive $B \to X_c \ell \nu$ branching fractions and form factors will help reduce the dominant modeling uncertainties in the signal composition. More precise theoretical predictions within the HQE framework will further enhance the sensitivity of inclusive measurements to the CKM matrix element $|V_{cb}|$.

With the anticipated full Belle II data set of $50\,\mathrm{ab}^{-1}$, inclusive semileptonic measurements will reach unprecedented precision. These measurements will provide critical input to global fits of the CKM matrix and may help clarify the long-standing tension between inclusive and exclusive determinations of $|V_{cb}|$. Ultimately, such precision studies of flavor physics play a key role in probing the SM and searching for potential signs of physics beyond it.

Appendix

A.1 Additional Figures: Signal yields extraction

A.1.1 Post-fit Signal Yields of the fine q_e^2 and q_μ^2 in M_X bins

The postfit signal yields of q_ℓ^2 in fine bins of 1 GeV^2 $\in [1, 12]$ GeV^2 in the three coarse bins of the hadronic mass $M_X \in [0,\ 1.8,\ 2.7,\ 4.0]$ GeV. The yields are obtained separately in the electron and lepton channels. Initially, the yields are also obtained separately for the B^+ and B^0 modes but are later combined in the analysis when unfolding and measuring the branching ratio.

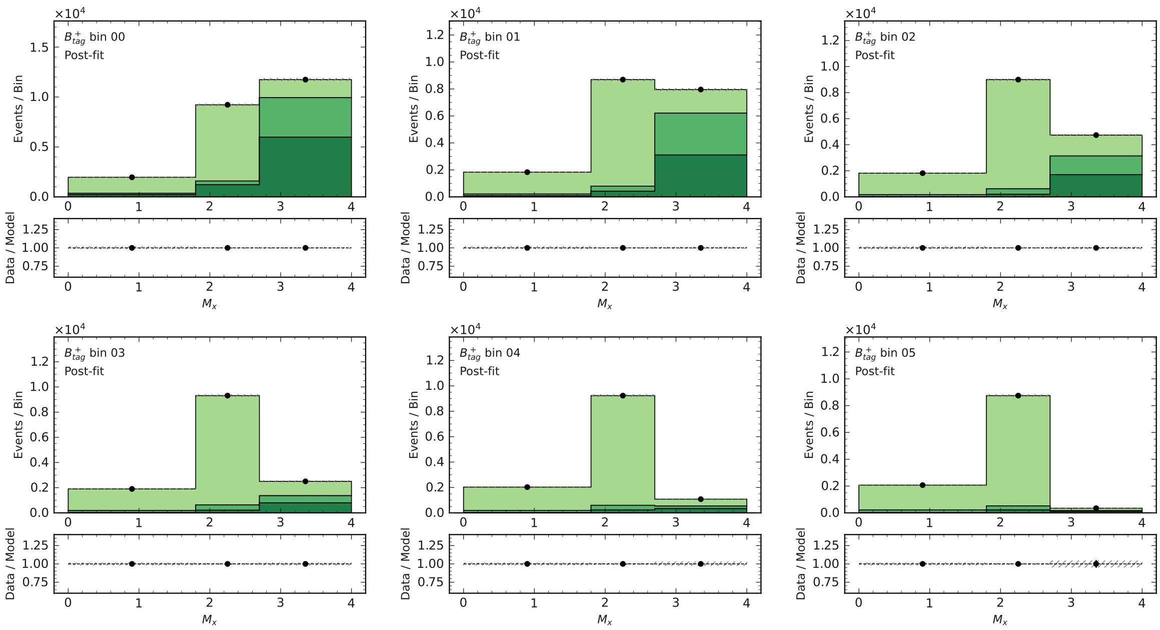

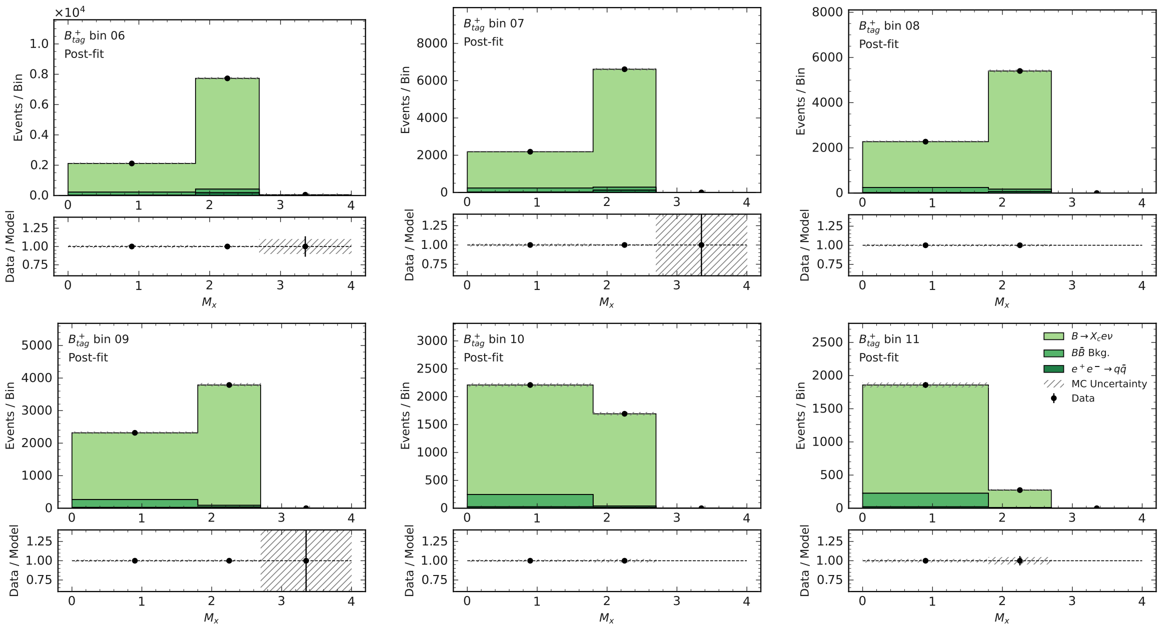

Figure A.1: Post-fit distributions of the fine q_e^2 bins within $0 \leq q_e^2 \leq 12\,\mathrm{GeV}^2$ in $1\,\mathrm{GeV}^2$ bins each for B^+, obtained from fits performed in three coarse M_X intervals: $[0, 1.8, 2.7, 4.0]$ GeV. In the plot, `bin 00` refers to the q_e^2 interval $[0, 1]\,\mathrm{GeV}^2$, `bin 01` refers to the q_e^2 interval $[1, 2]\,\mathrm{GeV}^2$ and so on.

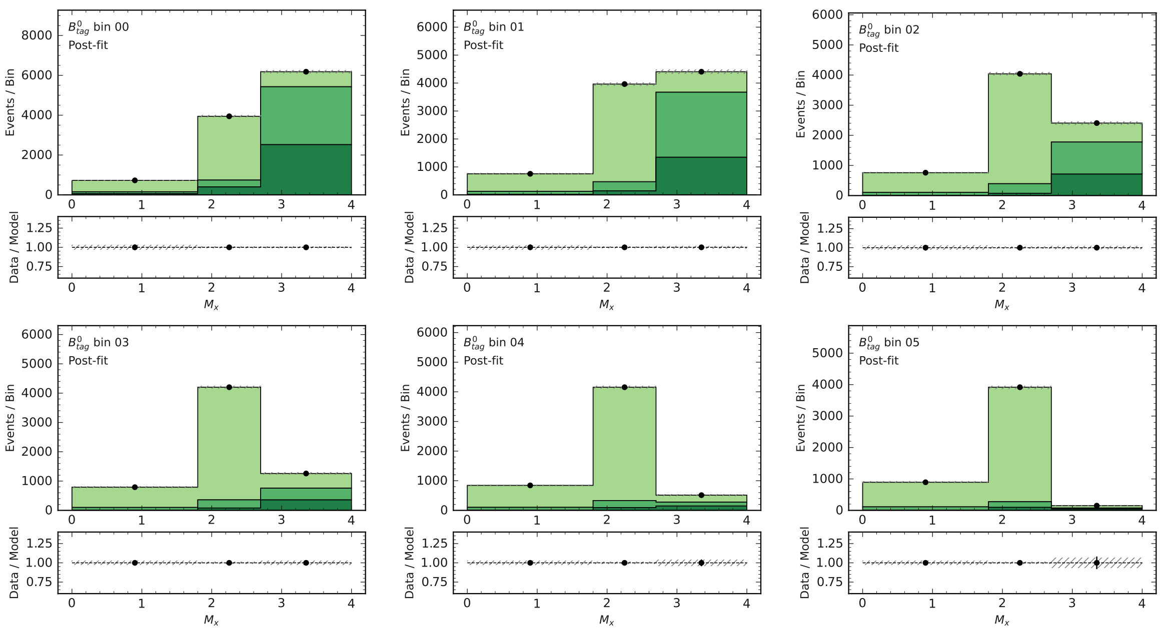

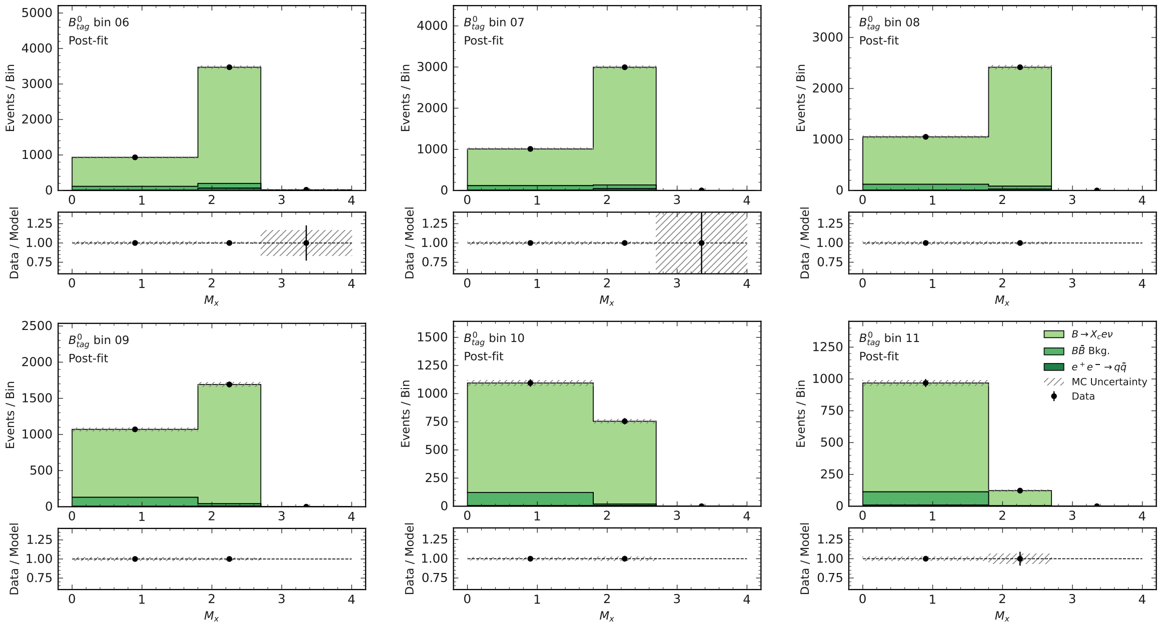

Figure A.2: Post-fit distributions of the fine q_e^2 bins within $0 \leq q_e^2 \leq 12\,\mathrm{GeV}^2$ in $1\,\mathrm{GeV}^2$ bins each for B^0, obtained from fits performed in three coarse M_X intervals: $[0, 1.8, 2.7, 4.0]\,\mathrm{GeV}$. In the plot, `bin 00` refers to the q_e^2 interval $[0, 1]\,\mathrm{GeV}^2$, `bin 01` refers to the q_e^2 interval $[1, 2]\,\mathrm{GeV}^2$ and so on.

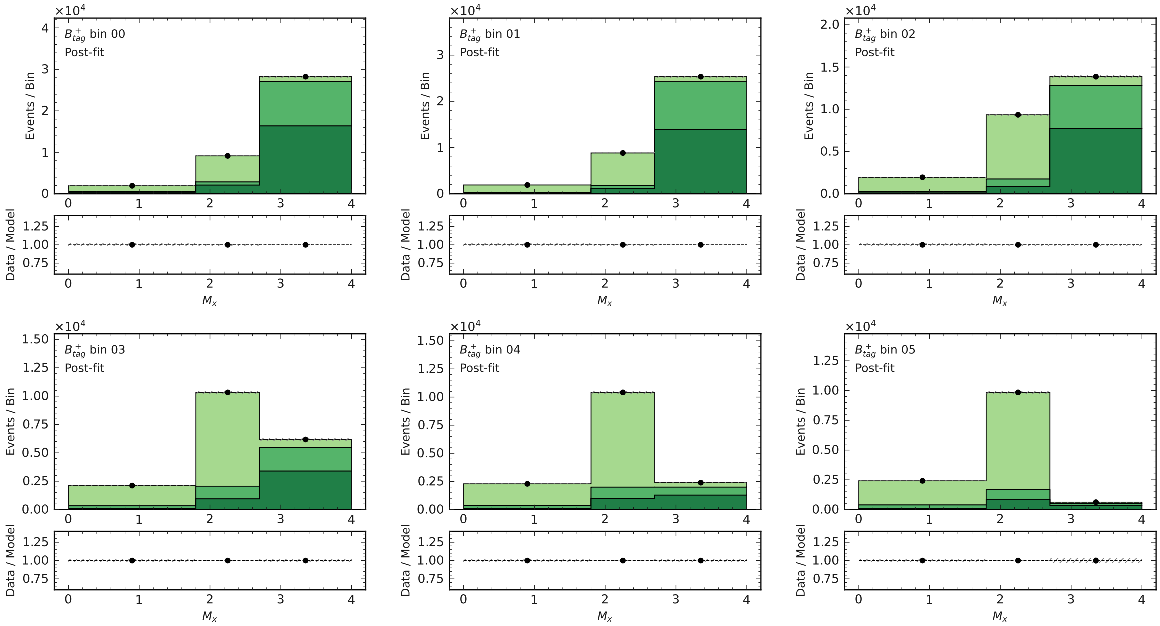

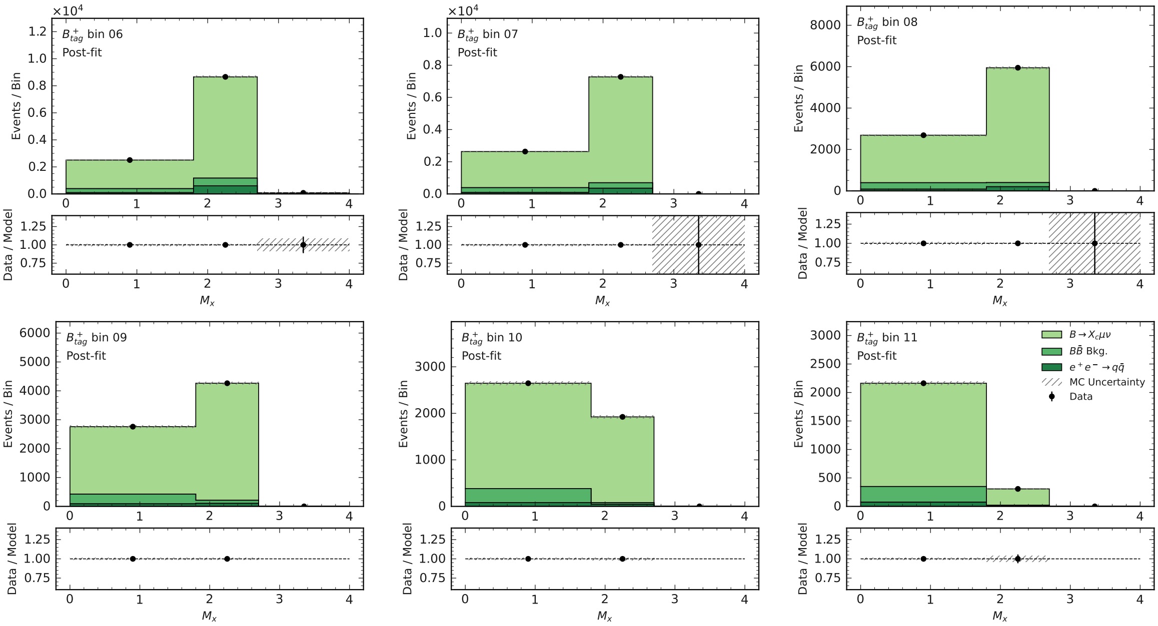

Figure A.3: Post-fit distributions of the fine q^2_μ bins within $0 \leq q^2_\mu \leq 12\,\mathrm{GeV}^2$ in $1\,\mathrm{GeV}^2$ bins each for B^+, obtained from fits performed in three coarse M_X intervals: $[0, 1.8, 2.7, 4.0]$ GeV. In the plot, `bin 00` refers to the q^2_μ interval $[0, 1]\,\mathrm{GeV}^2$, `bin 01` refers to the q^2_μ interval $[1, 2]\,\mathrm{GeV}^2$ and so on.

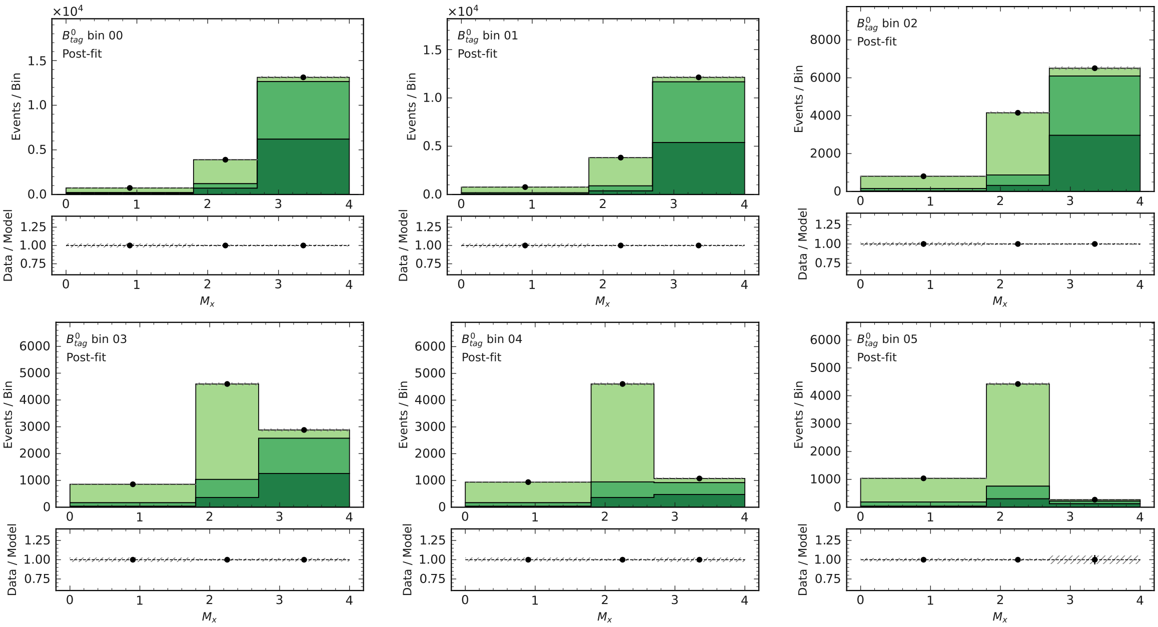

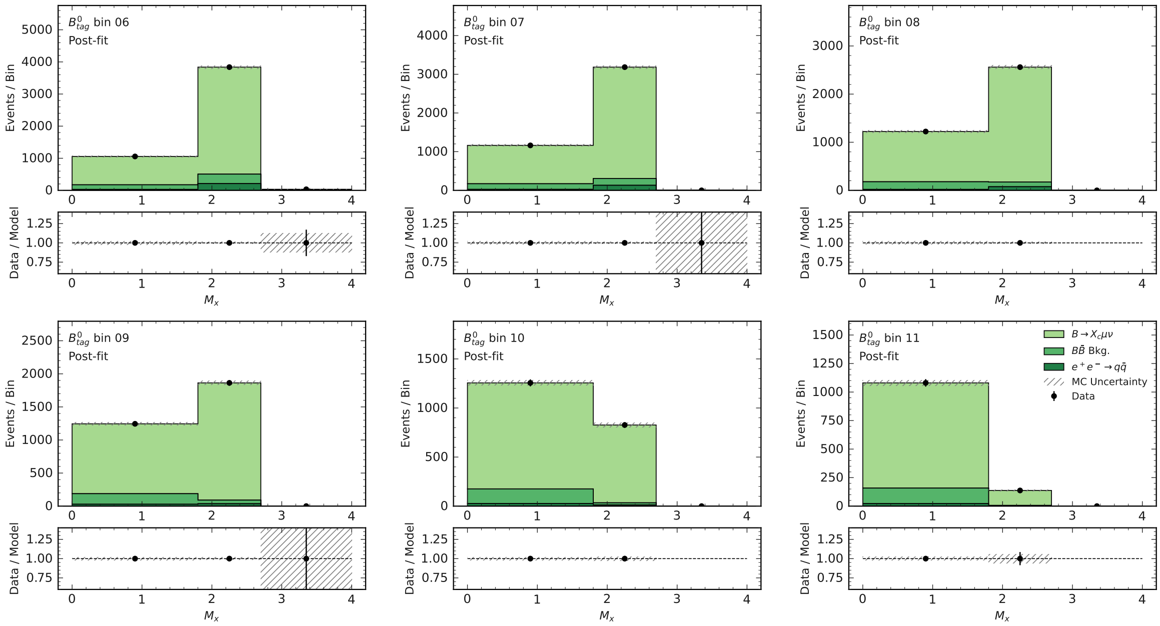

Figure A.4: Post-fit distributions of the fine q^2_μ bins within $0 \le q^2_\mu \le 12\,\mathrm{GeV}^2$ in $1\,\mathrm{GeV}^2$ bins each for B^0, obtained from fits performed in three coarse M_X intervals: $[0, 1.8, 2.7, 4.0]\,\mathrm{GeV}$. In the plot, `bin 00` refers to the q^2_μ interval $[0, 1]\,\mathrm{GeV}^2$, `bin 01` refers to the q^2_μ interval $[1, 2]\,\mathrm{GeV}^2$ and so on.

A.1.2 Post-fit Signal Yields of $\cos\ \theta_\ell$ in M_X bins

The postfit signal yields of $\cos\ \theta_\ell$ in 10 fine bins $\in [-1, 1]$ and each bin fit in the three coarse bins of the hadronic mass $M_X \in [0,\ 1.8,\ 2.7,\ 4.0]$ GeV. The yields are obtained separately in the electron and lepton channels. Initially, the yields are also obtained separately for the B^+ and B^0 modes but are later combined in the analysis when unfolding and measuring the branching ratio.

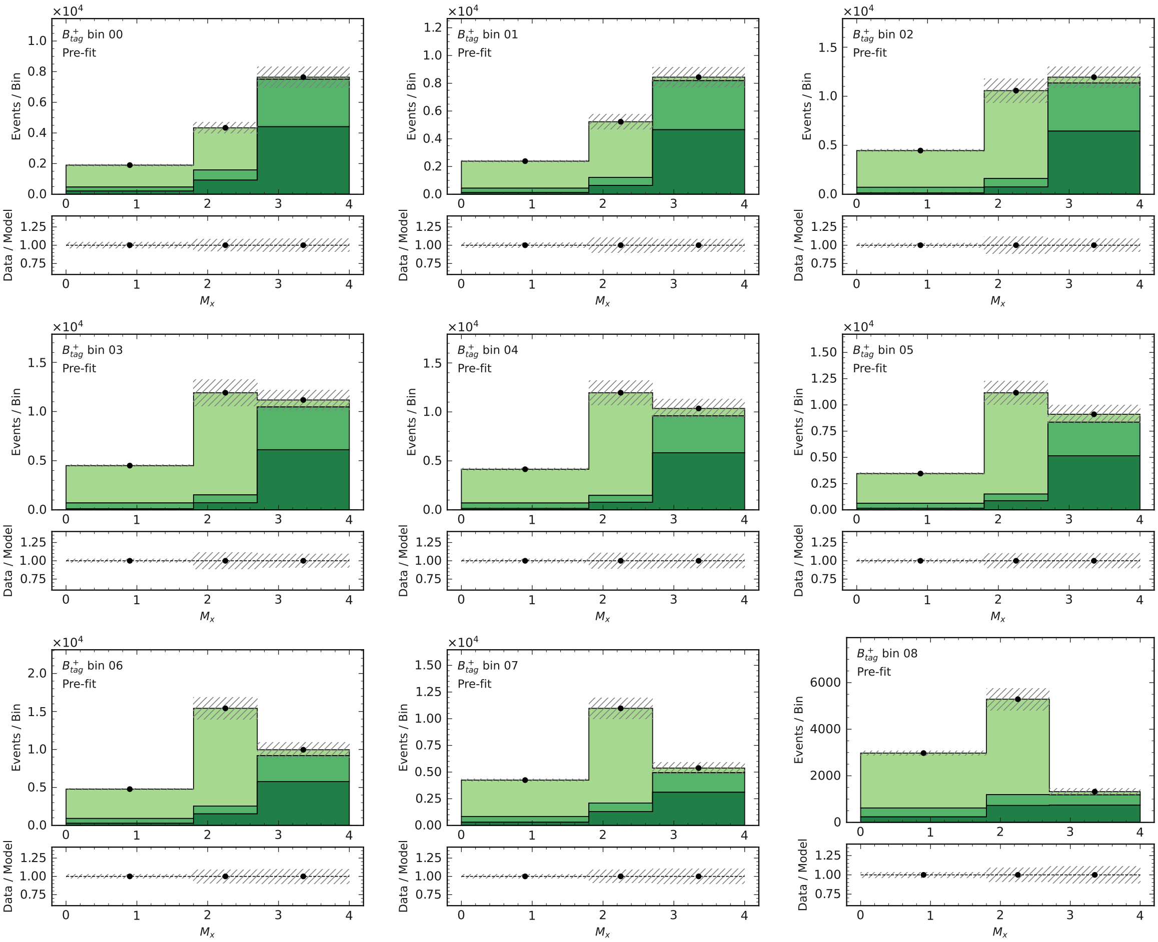

Figure A.5: Post-fit distributions of the fine $\cos\ \theta_e$ bins within $-1 \leq \cos\ \theta_e \leq 1$ in 10 equal bins for B^+, obtained from fits performed in three coarse M_X intervals: $[0, 1.8, 2.7, 4.0]$ GeV. In the plot, `bin 00` refers to the $\cos\ \theta_e$ interval $[-1.0, -0.77]$, `bin 01` refers to the $\cos\ \theta_e$ interval $[-0.77, -0.55]$ and so on.

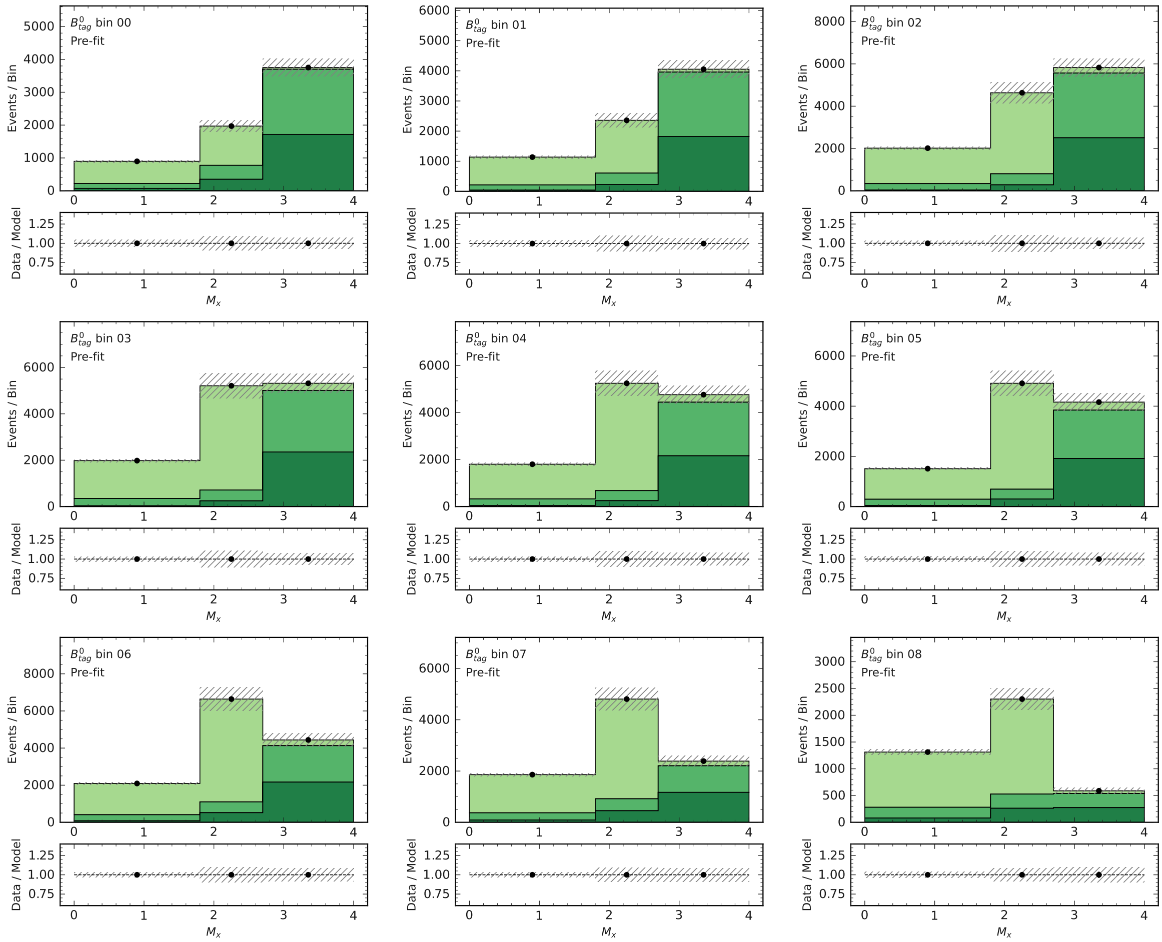

Figure A.6: Post-fit distributions of the fine cos θ_e bins within $-1 \leq \cos\ \theta_e \leq 1$ in 10 equal bins for B^0, obtained from fits performed in three coarse m_X intervals: $[0, 1.8, 2.7, 4.0]$ GeV. In the plot, `bin 00` refers to the cos θ_e interval $[-1.0, -0.77]$, `bin 01` refers to the cos θ_e interval $[-0.77, -0.55]$, and so on.

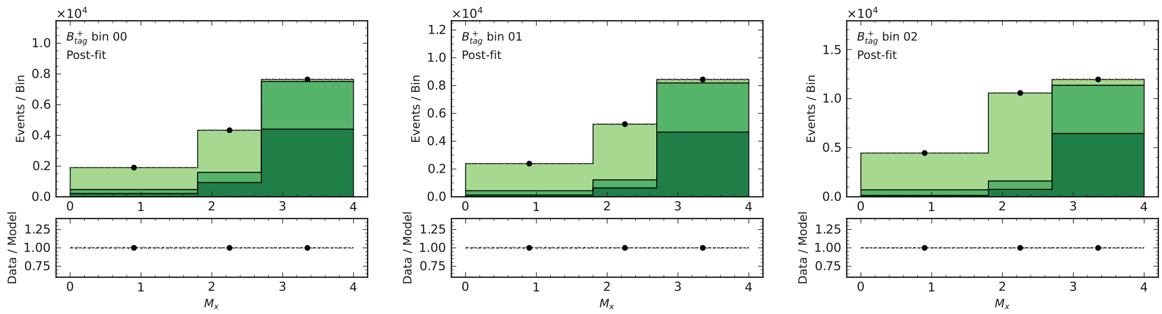

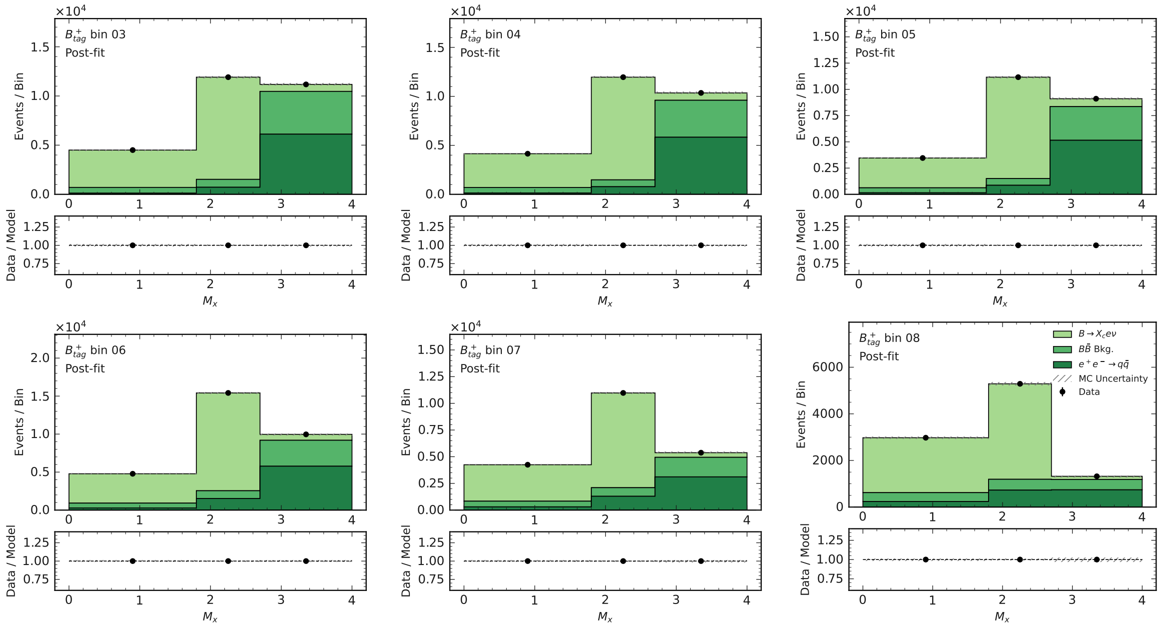

Figure A.7: Post-fit distributions of the fine cos θ_μ bins within $-1 \leq \cos\ \theta_\mu \leq 1$ in 10 equal bins for B^+, obtained from fits performed in three coarse m_X intervals: $[0, 1.8, 2.7, 4.0]$ GeV. In the plot, `bin 00` refers to the cos θ_μ interval $[-1.0, -0.77]$, `bin 01` refers to the cos θ_μ interval $[-0.77, -0.55]$ and so on.

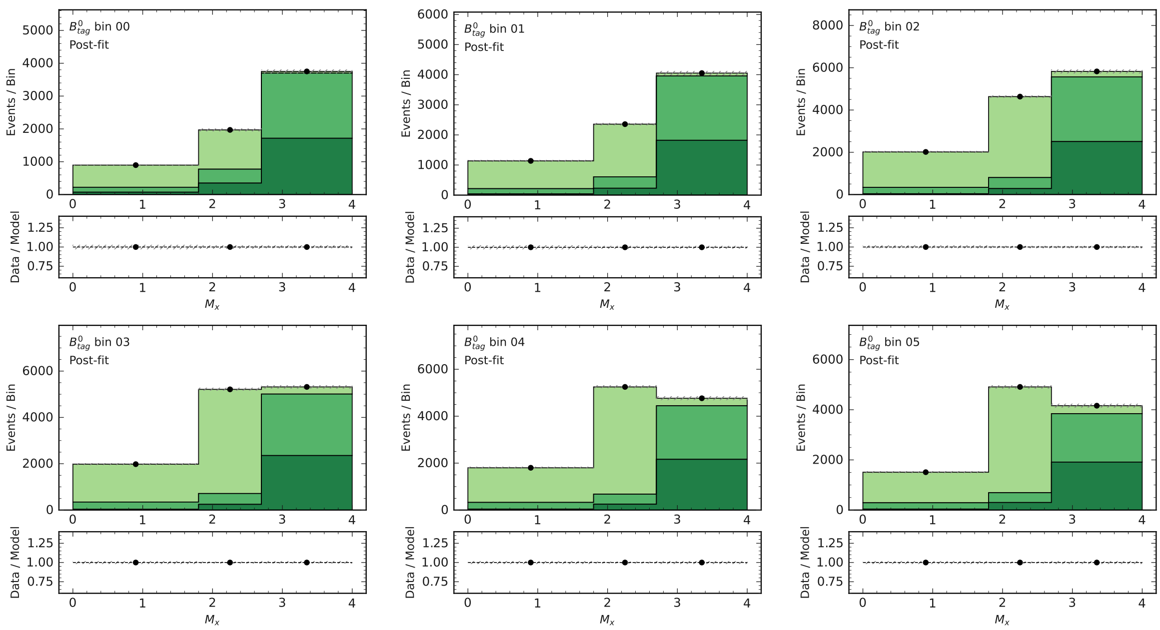

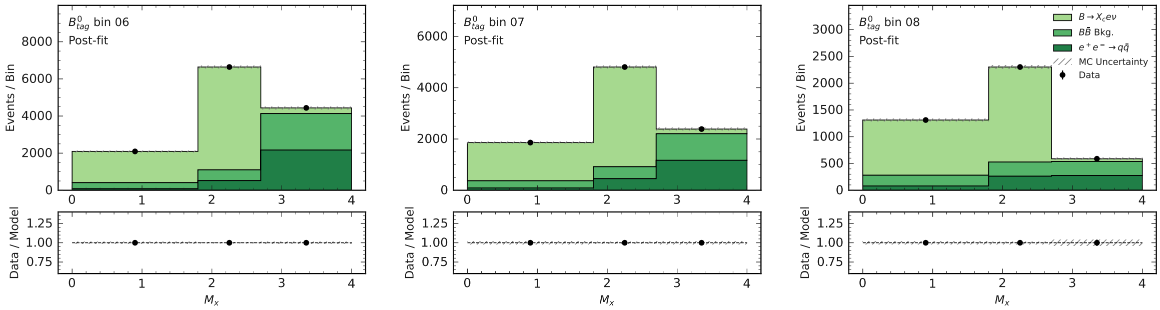

Figure A.8: Post-fit distributions of the fine $\cos\theta_\mu$ bins within $-1 \leq \cos\theta_\mu \leq 1$ in 10 equal bins for B^0, obtained from fits performed in three coarse m_X intervals: $[0, 1.8, 2.7, 4.0]$ GeV. In the plot, `bin 00` refers to the $\cos\theta_\mu$ interval $[-1.0, -0.77]$, `bin 01` refers to the $\cos\theta_\mu$ interval $[-0.77, -0.55]$ and so on.

A.2 Additional Figures: Unfolding

Fig. A.9 shows the signal reconstruction efficiency ε as a function of the lepton momentum p^B_ℓ for the electron and muon channels, comparing the cases where FSR is included using PHOTOS (red points) and where it is disabled (black points). The efficiencies are evaluated in bins of the lepton momentum threshold. The overall shape of the efficiency curve is similar for both channels, increasing with lepton momentum due to improved reconstruction and selection efficiency at higher momenta. The comparison between the two configurations demonstrates that the effect of FSR on the overall efficiency is small, with only minor deviations observed at higher momentum thresholds in the case of electrons where photon radiation can slightly modify the reconstructed lepton kinematics. In general, the efficiencies obtained with and without FSR remain consistent within uncertainties, indicating that the inclusion of FSR effects does not significantly alter the signal selection efficiency across the considered momentum range.

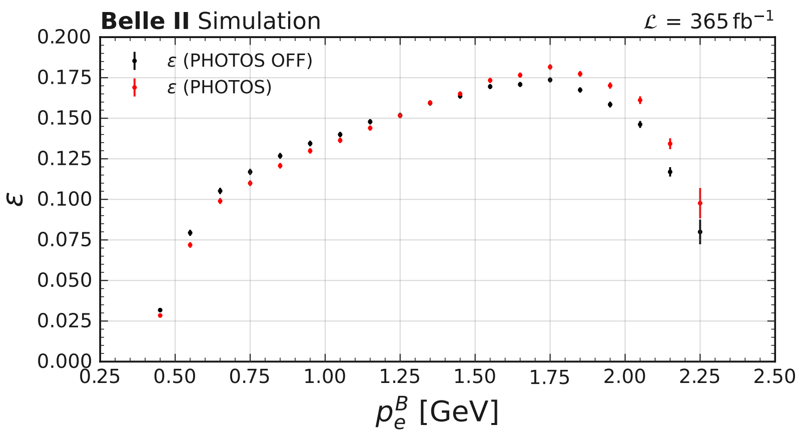

(a) ε_e in bins of the lepton momentum p^B_e with (PHOTOS in red) and without (PHOTOS OFF **in black**) the effect of FSR photons.

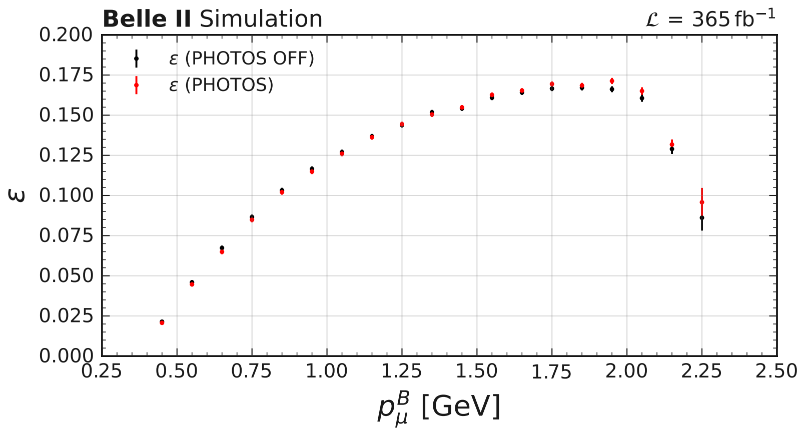

(b) ε_μ in bins of the lepton momentum p_μ^B with (PHOTOS in red) and without (PHOTOS OFF **in black**) the effect of FSR photons.

Figure A.9: Comparison of the ε in lepton momentum thresholds with and without the effect of the final state radiation (FSR) photons for the electron and muon channels.

Bibliography

[1] M. Fael, I. S. Milutin and K. K. Vos,
Kolya: An open-source package for inclusive semileptonic B decays,
SciPost Phys. Codeb. **55** (2025) 1, arXiv: `2409.15007 [hep-ph]` (cit. on pp. 2, 50).

[2] M. Thomson, *Modern Particle Physics*, Cambridge: Cambridge University Press, 2013 (cit. on p. 3).

[3] *The Belle II Experiment – Overview*, Online, Accessed: 02/02/2026, 2025,
URL: `https://www.belle2.de/en/belle-2-experiment` (cit. on p. 3).

[4] Belle II Software Group, *Introduction to* `basf2`, Online documentation for the Belle II analysis software framework `basf2`, describing its purpose and role in the Belle II data processing chain, 2026, URL: `https://software.belle2.org/development/sphinx/online_book/basf2/introduction.html` (cit. on pp. 3, 8).

[5] G. Cowan, *Statistical Data Analysis*, Available online,
Clarendon Press, Oxford University Press, 1998, URL:
`https://sherrytowers.com/cowan_statistical_data_analysis.pdf`
(cit. on pp. 3, 4).

[6] L. Heinrich, M. Feickert and G. Stark, *pyhf: v0.7.6*, version 0.7.6, Documentation, accessed 2025, 2025, URL: `http://pyhf.readthedocs.io/en/v0.7.6/` (cit. on p. 4).

[7] K. Cranmer, G. Lewis, L. Moneta, A. Shibata and W. Verkerke,
HistFactory: A tool for creating statistical models for use with RooFit and RooStats, (2012) (cit. on p. 4).

[8] A. Held, *Introduction to cabinetry: Constructing and steering pyhf models*,
Presentation at the pyhf Users and Developers Workshop 2023, CERN,
PDF available online, accessed 02/02/2026, 2023, URL: `https://indico.cern.ch/event/1294577/contributions/5689564/attachments/2764291/4814765/20231204_cabinetry_pyhf_workshop.pdf` (cit. on p. 4).

[9] G. Cowan, K. Cranmer, E. Gross and O. Vitells,
Asymptotic formulae for likelihood-based tests of new physics,
The European Physical Journal C **71** (2011), ISSN: 1434-6052,
URL: `http://dx.doi.org/10.1140/epjc/s10052-011-1554-0` (cit. on p. 5).

[10] T. Ilias, *Presentation at analysis tools meeting*,
`https://indico.belle2.org/event/12666/`, Accessed: 2025-02-06, 2024
(cit. on p. 5).

[11] *SysVar documentation*, https://sysvar.belle2.org/, Accessed: 14th March 2026, 2023, URL: https://sysvar.belle2.org/ (cit. on pp. 5, 41).

[12] Halbleiterlabor der Max-Planck-Gesellschaft, *BELLE II detector*, Web page describing the Belle II detector, 2026, URL: https://www.hll.mpg.de/2879447/BelleDetector (cit. on p. 7).

[13] EvtGen Collaboration, *EvtGen Documentation*, Official online documentation for the EvtGen heavy-flavour event generator, 2026, URL: https://evtgen.hepforge.org/doc/ (cit. on p. 8).

[14] E. Barberio, B. van Eijk and Z. Was, *Photos: A universal Monte Carlo for QED radiative corrections in decays*, Computer Physics Communications **66** (1991) 115, Monte Carlo program for QED radiative corrections in particle decays, URL: https://www.sciencedirect.com/science/article/pii/001046559190012A (cit. on pp. 8, 18, 35).

[15] Geant4 Collaboration, *Geant4 Documentation*, Documentation portal of the Geant4 toolkit, with user guides, reference manuals and examples, 2026, URL: https://geant4.web.cern.ch/docs/ (cit. on p. 8).

[16] M. Liu, N. Rout, K. Trabelsi and V. S. Vobbilisetti, *Hadronic FEI calibration with $D^{(*)}\pi$ samples*, tech. rep., Belle II Internal Note: Belle II Collaboration, 2023, URL: https://docs.belle2.org/pub_data/documents/127/ (cit. on p. 8).

[17] T. Martinov et al., *Measurement of inclusive $B \to X_u \ell \nu$ partial branching fractions and $|V_{ub}|$ at Belle II*, Belle II Internal Note, 2025, URL: https://docs.belle2.org/pub_data/documents/4594/ (cit. on p. 8).

[18] M. Angelsmark et al., *Inclusive search for the Weak Annihilation contribution to Charmless Semileptonic B Decays at Belle II*, Belle II Internal Note, 2023, URL: https://docs.belle2.org/pub_data/documents/70/ (cit. on p. 8).

[19] Belle II Collaboration, *BELLE2-TALK-2025-144*, Belle II internal talk, 2025, URL: https://docs.belle2.org/files/4690/BELLE2-TALK-2025-144/4/BELLE2-TALK-2025-144.pdf (cit. on p. 9).

[20] T. Keck et al., *The Full Event Interpretation: An Exclusive Tagging Algorithm for the Belle II Experiment*, Computing and Software for Big Science **3** (2019) 6, URL: https://doi.org/10.1007/s41781-019-0021-8 (cit. on p. 10).

[21] Belle II Collaboration, *Full Event Interpretation*, Belle II Analysis Software Framework (basf2) documentation, 2024, URL: https://software.belle2.org/development/sphinx/online_book/basf2/fei.html (cit. on p. 10).

[22] H. A. Junkerkalefeld, *Tests of lepton universality in the rates of inclusive semileptonic B-meson decays at Belle II*, PhD thesis: Rheinische Friedrich-Wilhelms-Universität Bonn, 2024, URL: https://hdl.handle.net/20.500.11811/11710 (cit. on p. 12).

[23] Heavy Flavor Averaging Group (HFLAV) — Olivier Schneider,
HFLAV perspective on b-hadron production fractions,
https://indico.cern.ch/event/628495/contributions/2571557/attachments/1453838/2245615/HFLAV_fractions_OS_04may2017.pdf,
Presentation at the LHC HF WG meeting, CERN, May 4 2017, 2017 (cit. on p. 38).

[24] F. U. Bernlochner, S. Duell, Z. Ligeti, M. Papucci and D. J. Robinson,
Das Ist Der HAMMER: Consistent New Physics Interpretations of Semileptonic Decays,
Eur. Phys. J. C **80** (2020) 883, ISSN: 1434-6044, 1434-6052, arXiv: 2002.00020 [hep-ph],
URL: http://arxiv.org/abs/2002.00020 (visited on 25/09/2023) (cit. on p. 42).

[25] F. U. Bernlochner et al.,
Constrained Second-Order Power Corrections in HQET: $R(D^{(*)})$, $|V_{cb}|$, and New Physics,
Phys. Rev. D **106** (2022) 096015, ISSN: 2470-0010, 2470-0029,
arXiv: 2206.11281 [hep-ph],
URL: http://arxiv.org/abs/2206.11281 (visited on 25/09/2023) (cit. on p. 42).

[26] F. U. Bernlochner, Z. Ligeti and D. J. Robinson,
Model Independent Analysis of Semileptonic B Decays to D^{**} for Arbitrary New Physics,
Phys. Rev. D **97** (2018) 075011, ISSN: 2470-0010, 2470-0029,
arXiv: 1711.03110 [hep-ph],
URL: http://arxiv.org/abs/1711.03110 (visited on 25/09/2023) (cit. on p. 42).

List of Figures

List of Tables